Dynamic Modeling of a Small Autonomous Hydrofoil Vessel

Heejip Moon

Thesis submitted to the Faculty of the
Virginia Polytechnic Institute and State University
in partial fulfillment of the requirements for the degree of

Master of Science
in
Electrical Engineering

Daniel J. Stilwell, Chair
Stefano Brizzolara
Thinh T. Doan

December 19, 2023
Blacksburg, Virginia

Keywords: Hydrodynamics, vehicle dynamics, nonlinear dynamics, model validation, unmanned marine vehicles, marine system identification and modeling, motion control

Dynamic Modeling of a Small Autonomous Hydrofoil Vessel

Heejip Moon

(ABSTRACT)

This thesis presents the development of a six degree of freedom nonlinear dynamic model for a single-mast fully submerged hydrofoil vehicle. The aim of the model is to aid in evaluating various model-based controllers for autonomous operation by simulating their performance before implementation in the field. Initially, first principles approach is employed to develop an approximate dynamic model of the vehicle. Prediction of the vehicle motion using the first principles model is then compared with the data from the tow tank experiments to assess the accuracy of the assumptions made in estimating the hydrofoil performance. Additionally, the dynamic model is adjusted to reflect the measured hydrodynamic forces in the tow tank tests. Utilizing the modified dynamic model to simulate the vehicle motion, an initial height controller is designed and tuned in field trials until stable foiling state was achieved. We evaluate the field results and discuss the limitation of employing steady-state tow tank data in establishing the vehicle dynamic model.

Dynamic Modeling of a Small Autonomous Hydrofoil Vessel

Heejip Moon

(GENERAL AUDIENCE ABSTRACT)

This thesis presents the development of a model describing the motion of a hydrofoil vehicle. The craft uses hydrofoils which act like conventional airplane wings that work in water instead of air to lift the hull fully out of the water. In order to maintain a set height above the water and direction of travel, the vehicle needs some form of a controller for autonomous operation. The purpose of the vehicle model is to aid in development of these controllers by simulating and evaluating their performance before implementation in the field. Initially, forces acting on the vehicle are approximated using fundamental hydrodynamic theory. The theoretical model is then compared with experimental data to assist in characterization of the hydrofoils. Building upon the measured test data, we create a preliminary height controller in simulation and conduct field trials to achieve stable foiling state.

Acknowledgments

I would like to thank my parents, Jongin and Seunghee Moon, and my brother, Heejun, for their love and support through out my time in Virginia Tech. I would like to thank Charles Watson, a research associate at Center for Marine Autonomy and Robotics, for his help in design and fabrication of components required for the hydrofoil vehicle and tow tank tests. I would also like to thank all my colleagues in the Center for Marine Autonomy and Robotics. In particular, I would like to thank Gwyneth Steel for her help in implementing the autonomy software, and Hugh Dougherty, Hans He, Stephen Krauss and Mingyu Kim for their help in field testing. I would like to thank Dr. Thinh T. Doan for his insight and taking the time to serve on my committee. I would like to thank Dr. Stefano Brizzolara for all his help and guidance with vehicle dynamics and hydrodynamics. Lastly, I would like to thank my advisor Dr. Daniel J. Stilwell for this research opportunity and for his invaluable guidance and support during this thesis.

Contents

List of Figures

List of Tables

List of Abbreviations

AVL Autonomous Vehicle Library

CAD Computer-Aided Design

CoB Center of Buoyancy

CoD Coefficient of Drag

CoG Center of Gravity

CoL Coefficinet of Lift

DoF Degree of Freedom

NACA National Advisory Committee for Aeronautics

PID Proportional-Integral-Derivative

Chapter 1

Introduction

Compared to conventional surface vessels, hydrofoil vehicles offer several advantages in speed, efficiency, and maneuverability. During normal operation, hydrofoils elevate the hull above the water, reducing drag and enabling higher speeds for a given power input. Additionally, when the hull is lifted clear of the water surface, the vehicle can navigate above waves in rough seas, surf zones, and other high disturbance areas. In fully submerged hydrofoils, most of the trailing wake is generated by the struts connecting the hull to the foils, rather than the hull itself, which significantly reduces the visible wake. Since only the hydrofoils and propulsion unit need to be submerged to control the craft, the vehicle can operate at shallow depth if necessary. These benefits serve as the main motivation for the given research task of developing an autonomous vehicle from an existing commercial hydrofoil platform.

To achieve autonomy, a controller is required to command the vehicle's attitude and sustain its foiling state. Employing a high fidelity vehicle dynamics model can aid in developing such vehicle controller by simulating and assessing different control algorithms before field implementation. This approach reduces the time needed for field tuning the control system and enables an objective comparison of various controllers' performance under repeatable conditions. To validate the hydrodynamic coefficients used in the vehicle dynamics model, tow tank studies have been conducted for different vehicle types including surface vessel [17], amphibious vehicle [15], foil assisted monohull [18], and autonomous underwater vehicle [7]. However, a 6 degree of freedom (DoF) dynamic model tested at full-scale has not yet been

investigated for a hydrofoil craft. The main contribution of this work is the verification of a first principles dynamic model utilizing the results from tow tank trials. We compare the applied forces and moments obtained from the vehicle approximation model derived with fundamental hydrodynamic principles to the experimentally measured data in the tow tank. Subsequently, we adjust the first principles model to reflect the measured forces then employ the modified model to create an initial proportional-integral-derivative (PID) controller for height and pitch motion. The gains of the controllers are further tuned during field testing. Using the result of the field trials, we assess the limitation of the assumptions made in the 6 DoF model which is constructed using steady-state tow tank results.

The thesis is organized as follows. General overview of the hydrofoil craft and its modification is provided in Chapter 2. The components of the dynamic model based in first principles are laid out in Chapter 3. Chapter 4 outlines the experimental test fixture in the tow tank and compares the collected results to the theoretical predictions. The modified dynamic model fitted to the tow data, the simulated PID height controller, and the controller's performance during field trials are discussed in Chapter 5. Finally, the concluding remarks are provided in Chapter 6. Much of the contents in Chapter 2 through 6 are adapted from the conference papers *Development of a Dynamic Model of Small Autonomous Hydrofoil Craft* by Heejip Moon, Gwyneth Steel, Hugh Dougherty, Daniel Stilwell, and Stefano Brizzolara [10] and *Experimental Study of a Preliminary Height Controller for a Small Autonomous Hydrofoil Craft* by Heejip Moon, Daniel Stilwell, and Stefano Brizzolara [11].

Chapter 2

Vehicle Overview

2.1 Original Vehicle

For this study, the electric hydrofoil platform from Lift Foils shown in Figure 2.1 was chosen as the basis for the autonomous vehicle. The eFoil features a single-mast design housing an

Figure 2.1: eFoil from Lift Foils modified with control flaps and additional electronics for autonomous operation

integrated electric motor and propeller assembly, and fully submerged fore and aft hydrofoils. It is capable of reaching up to 30 mph and 100 minutes of maximum ride time, and can accommodate a rider weighing up to 250 lbs. Designed for recreational use, a human operator

riding on top of the eFoil can control the craft's pitch and roll by shifting their weight fore or aft and side to side, while the motor speed is regulated via a waterproof handheld controller. As this is a commercial vehicle, the proprietary geometry of the submerged hydrofoils were not made available and the complex shape of the foils as shown in Figure 2.2 posed challenges in accurately measuring and approximating their hydrodynamic performance.

(a) (b)

Figure 2.2: (a) Trapezoidal fore foil with span wise anhedral curve, (b) Trapezoidal aft foil with maximum thickness of 1 cm

2.2 Modification

To control the vehicle attitude, two different actuation methods were explored. Similar to how a human rider operates the eFoil, a system of moving masses can be added on top of the board to control the pitch and roll of the craft. This method requires no modification to the submerged hydrofoil sections while utilizing existing mounting points on the board for securing equipment. However, a significant amount of additional weight or actuator travel distance is needed to influence the vehicle's motion. Alternatively, control flaps can be added to the submerged foils in order to directly affect the lift and drag forces. The benefit of this

approach is that it requires much less actuation effort compared to a moving mass system and offers more space to mount additional payload on top of the board. However, due to the thin profile of the foils and their carbon fiber construction, integrating the actuator assembly into the hydrofoils without compromising their strength required more design time compared to the moving mass concept. As a result, the moving mass actuation was initially pursued using off-the-shelf components to quickly field test the vehicle and obtain data for comparison to the theoretical dynamic model. Simultaneously, the control flap mechanism was being tested and developed for implementation further down the timeline. In practice, however, it was found that the fastest readily available commerical linear actuator lacked the bandwidth to compensate for the vehicle's fast dynamics. To make the moving mass system work, a custom actuator package would need to be developed which would take considerable time and effort, contradicting its original purpose as a quick solution for controlling the vehicle. Following rounds of field tests with moving mass actuators, the decision was made to concentrate solely on implementing the control flap actuation. Consequently, this paper focuses on the results of flap actuation for vehicle control, but readers can find additional details on the rigid body dynamics derived for a moving mass system in Appendix A.

For flap actuation, the original craft was modified by adding servo driven elevator and rudder surfaces on the aft hydrofoil as shown in Figure 2.3. The flap placement was determined by the ease of mounting and modifying the tail hydrofoil assembly, as well as the large moment arm provided by the distance from the stern wing to the vehicle's center of gravity (CoG). The elevator flaps are split down the middle with two independently controlled sides which generate roll moment when rotated in opposite directions. Given the challenge of packaging a flap hinge mechanism due to the thin trailing edge of the aft hydrofoil, the elevator flaps are affixed to the foil surface with tape for quick implementation and testing without modifying and risking delamination of the carbon fiber wing. A single rudder flap, positioned behind

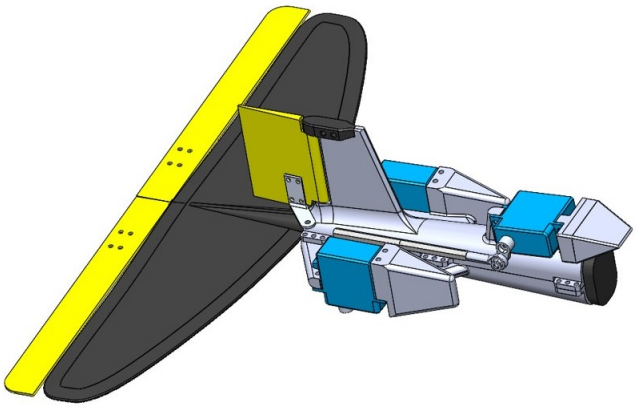

Figure 2.3: 3D printed elevator and rudder flap assembly mounted on the aft hydrofoil

the propulsor, is used to induce both roll and yaw moment. All three flaps are connected to each of the servo control arm by a linkage with ball joint ends. The servos and the rudder flap pivot are secured onto 3D printed top and bottom shells that clamp around the carbon fiber stem connecting the aft foil to the fore foil.

To manipulate the propeller thrust, the factory handheld controller was modified with a throttle servo to command the motor speed as illustrated in Figure 2.4. The original con-

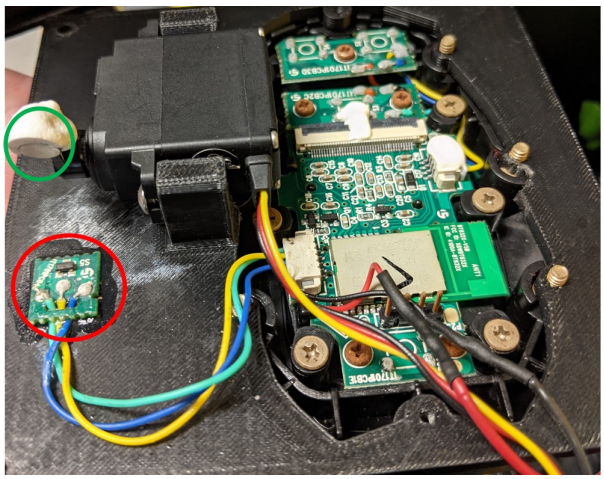

Figure 2.4: Throttle controller board with hall effect sensor circled in red and servo driven permanent magnet circled in green

troller utilized a hall effect sensor to measure the field strength of a magnet which was affixed

to a movable trigger lever. As the magnet moves closer to the sensor, an increasing throttle signal is sent to the motor controller over a Bluetooth connection. Rather than reproducing this specific throttle signal or modifying the proprietary motor controller, the original electronics from the handheld remote is reused in a 3D printed housing where the distance between the magnet and the hall effect sensor is controlled by a servo.

Lastly a waterproof enclosure for electronics computing actuator commands, attitude, heading, GPS location, body angular rate, and linear acceleration, is mounted near the bow of the eFoil. Layout of the electronic hardware used for autonomy is illustrated in Figure 2.5. The sensors and actuators are connected to a single board computer running the Au-

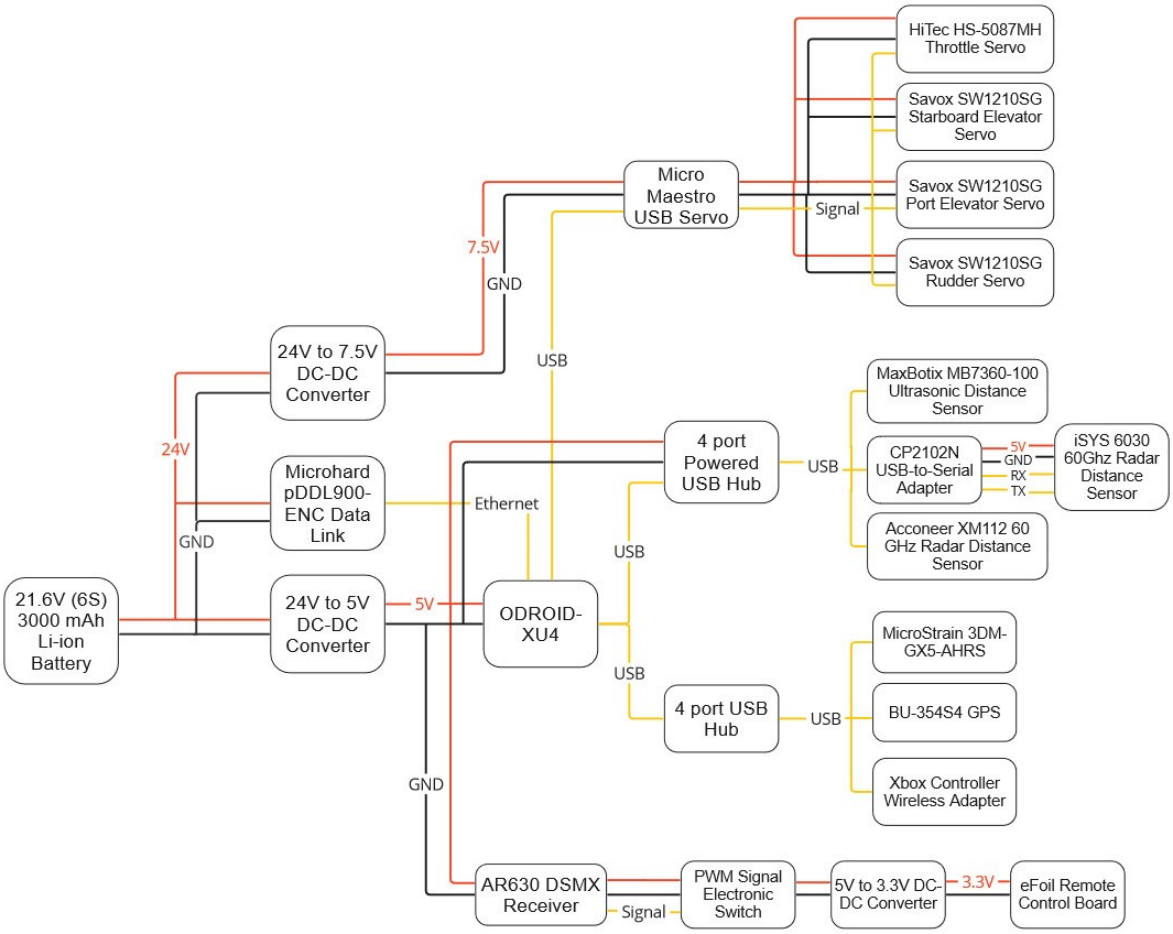

Figure 2.5: Diagram of the added electronic hardware utilized for autonomy

tonomous Vehicle Library (AVL), developed by Center for Marine Autonomy and Robotics. AVL leverages tools from the open-source Robotic Operating System to facilitate communication between all the electronic hardware, compute controller outputs, and log measured sensor data and actuator commands. For field tests, a 2.4 GHz radio data link is employed to establish a remote connection to the onboard vehicle computer for craft operation and log file transfer. Additionally, a joystick controller can be used to directly send commands at close distances. For safety, a separate radio receiver, paired to an onshore transmitter, is used in case the radio data link to the onboard computer fails. If the user toggles a switch on the transmitter or if the onboard receiver moves out of range, the power to the eFoil throttle controller board is cut off, stopping the propeller motor. Initially, three different distance sensors were assessed for measuring the board's height above the water. Ultimately, the radar-based Acconeer XM112 distance module, housed in a waterproof enclosure with a hydrophobic coating, proved most effective. During field tests, this module exhibited high enough update rate to capture foiling height during quick movements, could measure through thin layer of water and hydrophobic coating, could be easily powered through USB port due to low power consumption, and had wide enough detection angle to recognize the water surface as the vehicle rolled or pitched to one side.

Chapter 3

First Principles Dynamic Model

3.1 Vehicle Coordinate Frames

Following the convention for describing 6 DoF rigid body motion in [4] and [12], the body and inertial reference frame are arranged as shown in Figure 3.1 for the hydrofoil craft. The

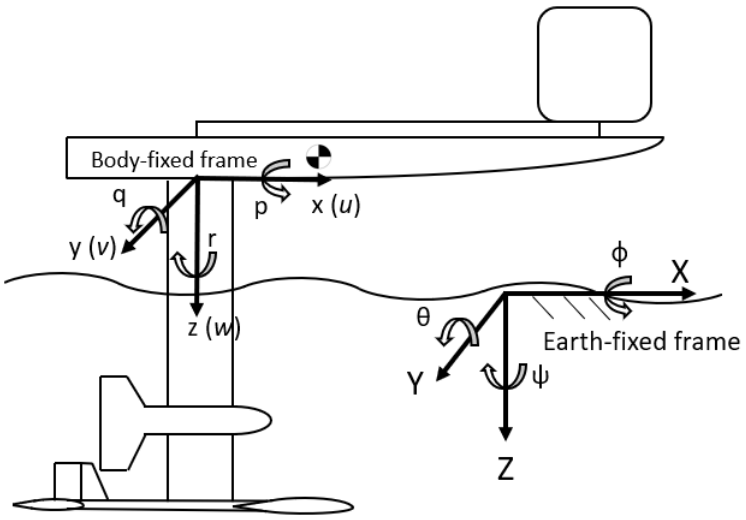

Figure 3.1: Frame of reference used for the hydrofoil craft and the associated linear and angular velocities

origin of the moving body frame is located at the bottom of the board and center of the mast. The zero for the fixed inertial frame Z axis is located at the water line. In this case the body-fixed origin is not coincident with either CoG or center of buoyancy (CoB), but

rather chosen to be a fixed physical location on the vehicle so that it remains unaffected by additional payload weight or varying submerged volume. The body origin still keeps the vehicle symmetry about the xz plane and its location in the inertial Z coordinate directly indicates the foiling height of the craft. The vehicle motion is defined using body frame linear and angular velocities $\nu = \begin{bmatrix} u & v & w & p & q & r \end{bmatrix}^T$ where u, v, and w are the body-fixed linear velocities along the x, y, and z axis, respectively, and p, q, and r are the angular rates about the same axis. The inertial position and orientation of the model is described by $\eta = \begin{bmatrix} X & Y & Z & \phi & \theta & \psi \end{bmatrix}^T$ where X, Y, and Z are the inertial frame coordinates of the body frame origin, and ϕ, θ, and ψ are the Euler angles corresponding to roll, pitch, and yaw.

The vectors in the fixed inertial frame can be related to the vectors in the moving body frame by three principal rotation about the Z, Y, and X axes with their respective Euler angles. Using this rotation sequence, the linear body-fixed velocities $\nu_1^T = \begin{bmatrix} u & v & w \end{bmatrix}$ can be transformed to the inertial frame linear velocities $\dot{\eta_1}^T = \begin{bmatrix} \dot{X} & \dot{Y} & \dot{Z} \end{bmatrix}$ by the rotation matrix J_1 where

$$\begin{bmatrix} \dot{X} \\ \dot{Y} \\ \dot{Z} \end{bmatrix} = \begin{bmatrix} \cos\psi\cos\theta & -\sin\psi\cos\phi + \cos\psi\sin\theta\sin\phi & \sin\psi\sin\phi + \cos\psi\cos\phi\sin\theta \\ \sin\psi\cos\theta & \cos\psi\cos\phi + \sin\phi\sin\theta\sin\psi & -\cos\psi\sin\phi + \sin\theta\sin\psi\cos\phi \\ -\sin\theta & \cos\theta\sin\phi & \cos\theta\cos\phi \end{bmatrix} \begin{bmatrix} u \\ v \\ w \end{bmatrix}$$

$$\dot{\eta_1} = J_1(\eta)\,\nu_1 \tag{3.1}$$

The angular velocities in the inertial frame is related to the body-fixed rotational velocities

by the rotation matrix J_2 and velocity vectors $\nu_2^T = \begin{bmatrix} p & q & r \end{bmatrix}$ and $\dot{\eta_2}^T = \begin{bmatrix} \dot{\phi} & \dot{\theta} & \dot{\psi} \end{bmatrix}$ where

$$\begin{bmatrix} \dot{\phi} \\ \dot{\theta} \\ \dot{\psi} \end{bmatrix} = \begin{bmatrix} 1 & \sin\phi\tan\theta & \cos\phi\tan\theta \\ 0 & \cos\phi & -\sin\phi \\ 0 & \sin\phi/\cos\theta & \cos\phi/\cos\theta \end{bmatrix} \begin{bmatrix} p \\ q \\ r \end{bmatrix} \tag{3.2}$$

$$\dot{\eta_2} = J_2(\eta)\,\nu_2$$

Because of the tangent terms in J_2, it is assumed that the pitch angle θ stays between -90° to 90°. This assumption is suitable for the scope of this thesis as the motion of the hydrofoil vehicle at extreme angles where the bow of the craft is pointed straight up or down is not of interest. Combining the rotation matrices for transnational and rotational velocities into one expression for 6 DoF motion yields

$$\dot{\eta} = \begin{bmatrix} J_1(\eta_2) & 0_{3\times3} \\ 0_{3\times3} & J_2(\eta_2) \end{bmatrix} \nu \tag{3.3}$$

$$\dot{\eta} = J(\eta_2)\,\nu$$

3.2 Rigid Body Dynamics

Using conservation of linear and angular momentum, the applied forces and moments on a rigid body can be related to the transitional and rotational velocities and accelerations. The equations of motion for the vehicle moving through a fluid can be represented as

$$(M_A + M_{RB})\dot{\nu} + (C_A + C_{RB})\nu + G = \tau \tag{3.4}$$

where M_{RB} and C_{RB} are the rigid body inertia and Coriolis-centripetal matrices, M_A and C_A are the hydrodynamic added inertia and added Coriolis-centripetal matrices, G is the weight and buoyancy vector, and τ is the external force and moment vector. The derivation of the rigid body motion equation (3.4) is found in Chapter 2.3 of [4].

We follow Fossen's formulation of the rigid body matrices M_{RB} and C_{RB} [4, pg. 26, 28] using the measured mass, CoG location, and inertia tensor of the craft about the body-fixed frame where vehicle symmetry across the xz plane is assumed. The CoG and weight of each components such as the board, battery, mast assembly, and electronics enclosure were measured individually. The approximate geometry of these components is then recreated in computer-aided design (CAD) software along with user specified density to match the measured weight and CoG. The simplified CAD models are then assembled in the body reference coordinate system to yield total vehicle CoG of [0.382 m, 0 m, 0.015 m] and total mass of 47.9 kg. The exact CoG location and weight of each components are listed in Appendix B Table B.1. Additionally, we can calculate the inertia tensor I_o

$$I_o = \begin{bmatrix} I_{xx} & I_{xy} & I_{xz} \\ I_{yx} & I_{yy} & I_{yz} \\ I_{zx} & I_{zy} & I_{zz} \end{bmatrix} = \begin{bmatrix} 8.230 & 0 & -3.785 \\ 0 & 17.215 & 0 \\ -3.785 & 0 & 12.733 \end{bmatrix} kg\,m^2 \tag{3.5}$$

from the CAD software as the component models were close enough approximation of the true part geometry, weight and CoG. Note that this model is created solely for estimating the moment of inertia as it does not reflect the actual foil shape with sufficient accuracy to be used for computational fluid dynamics studies. Using the total vehicle mass m, the inertia tensor I_o, and the coordinates of vehicle CoG in body-fixed frame $[x_G\,, y_G\,, z_G]$, the

rigid body inertia matrix is defined as

$$M_{RB} = \begin{bmatrix} m & 0 & 0 & 0 & m\,z_G & -m\,y_G \\ 0 & m & 0 & -m\,z_G & 0 & m\,x_G \\ 0 & 0 & m & m\,y_G & -m\,x_G & 0 \\ 0 & -m\,z_G & m\,y_G & I_{xx} & I_{xy} & I_{xz} \\ m\,z_G & 0 & -m\,x_G & I_{yx} & I_{yy} & I_{yz} \\ -m\,y_G & m\,x_G & 0 & I_{zx} & I_{zy} & I_{zz} \end{bmatrix} = \begin{bmatrix} 47.9 & 0 & 0 & 0 & 0.719 & 0 \\ 0 & 47.9 & 0 & -0.719 & 0 & 18.298 \\ 0 & 0 & 47.9 & 0 & -18.298 & 0 \\ 0 & -0.719 & 0 & 8.23 & 0 & -3.785 \\ 0.719 & 0 & -18.298 & 0 & 17.215 & 0 \\ 0 & 18.298 & 0 & -3.785 & 0 & 12.733 \end{bmatrix} \tag{3.6}$$

The centripetal and Coriolis forces experienced by the moving rigid body in respect to the Earth-fixed frame is calculated using the Coriolis-centripetal matrix expressed as

$$C_{RB} = \begin{bmatrix} 0 & 0 & 0 & m(y_Gq + z_Gr) & -m(x_Gq - w) & -m(x_Gr + v) \\ 0 & 0 & 0 & -m(y_Gp + w) & m(z_Gr + x_Gp) & -m(y_Gr - u) \\ 0 & 0 & 0 & -m(z_Gp - v) & -m(z_Gq + u) & m(x_Gp + y_Gq) \\ -m(y_Gq + z_Gr) & m(y_Gp + w) & m(z_Gp - v) & 0 & -I_{yz}q - I_{xz}p + I_{zz}r & I_{yz}r + I_{xy}p - I_{yy}q \\ m(x_Gq - w) & -m(z_Gr + x_Gp) & m(z_Gq + u) & I_{yz}q + I_{xz}p - I_{zz}r & 0 & -I_{xz}r - I_{xy}q + I_{xx}p \\ m(x_Gr + v) & m(y_Gr - u) & -m(x_Gp + y_Gq) & -I_{yz}r - I_{xy}p + I_{yy}q & I_{xz}r + I_{xy}q - I_{xx}p & 0 \end{bmatrix}$$

$$= \begin{bmatrix} 0 & 0 & 0 & 0.719\,r & -18.298\,q + 47.9\,w & -18.298\,r - 47.9\,v \\ 0 & 0 & 0 & -47.9\,w & 0.719\,r + 18.298\,p & 47.9\,u \\ 0 & 0 & 0 & -0.719\,p + 47.9\,v & -0.719\,q - 47.9\,u & 18.298\,p \\ -0.719\,r & 47.9\,w & 0.719\,p - 47.9\,v & 0 & 3.785\,p + 12.733\,r & -17.215\,q \\ 18.298\,q - 47.9\,w & -0.719\,r - 18.298\,p & 0.719\,q + 47.9\,u & -3.785\,p - 12.733\,r & 0 & 3.785\,r + 8.23\,p \\ 18.298\,r + 47.9\,v & -47.9\,u & -18.298\,p & 17.215\,q & -3.785\,r - 8.23\,p & 0 \end{bmatrix} \tag{3.7}$$

3.3 Added Mass and Inertia

As the submerged section of the vehicle moves through the water, it experiences an additional inertia referred to as added mass when some volume of the surrounding fluid is forced around the physical body. By using the assumption that the body in motion imparts energy to the otherwise stationary fluid, one can derive the fluid forces and moments acting on the vehicle

using the added mass inertia matrix defined as

$$M_A = \begin{bmatrix} X_{\dot{u}} & X_{\dot{v}} & X_{\dot{w}} & X_{\dot{p}} & X_{\dot{q}} & X_{\dot{r}} \\ Y_{\dot{u}} & Y_{\dot{v}} & Y_{\dot{w}} & Y_{\dot{p}} & Y_{\dot{q}} & Y_{\dot{r}} \\ Z_{\dot{u}} & Z_{\dot{v}} & Z_{\dot{w}} & Z_{\dot{p}} & Z_{\dot{q}} & Z_{\dot{r}} \\ K_{\dot{u}} & K_{\dot{v}} & K_{\dot{w}} & K_{\dot{p}} & K_{\dot{q}} & K_{\dot{r}} \\ M_{\dot{u}} & M_{\dot{v}} & M_{\dot{w}} & M_{\dot{p}} & M_{\dot{q}} & M_{\dot{r}} \\ N_{\dot{u}} & N_{\dot{v}} & N_{\dot{w}} & N_{\dot{p}} & N_{\dot{q}} & N_{\dot{r}} \end{bmatrix} \tag{3.8}$$

Although all 36 elements of M_A can be unique, a reasonable approximation for foiling vehicles is to assume that M_A is symmetric [4], leaving 21 independent terms. The notation $X_{\dot{v}}$ corresponds to the contribution the acceleration in body-fixed y axis has to the hydrodynamic force in the body-fixed x axis. The kinetic energy of the fluid pushed aside by the vehicle is then expressed with the body-fixed linear and angular velocities and the virtual inertial mass M_A as

$$T_A = \frac{1}{2}\nu^T M_A \nu \tag{3.9}$$

Kirchhoff's equations as found in Chapter 2.4 of [4] utilizes the expression for fluid kinetic energy to define the hydrodynamic added mass forces and moments τ_H as

$$\tau_H = \begin{bmatrix} \frac{d}{dt}\frac{\partial T_A}{\partial u} - r\frac{\partial T_A}{\partial v} + q\frac{\partial T_A}{\partial w} \\ \frac{d}{dt}\frac{\partial T_A}{\partial v} - p\frac{\partial T_A}{\partial w} + r\frac{\partial T_A}{\partial u} \\ \frac{d}{dt}\frac{\partial T_A}{\partial w} - q\frac{\partial T_A}{\partial u} + p\frac{\partial T_A}{\partial v} \\ \frac{d}{dt}\frac{\partial T_A}{\partial p} - w\frac{\partial T_A}{\partial v} + v\frac{\partial T_A}{\partial w} - r\frac{\partial T_A}{\partial q} + q\frac{\partial T_A}{\partial r} \\ \frac{d}{dt}\frac{\partial T_A}{\partial q} - u\frac{\partial T_A}{\partial w} + w\frac{\partial T_A}{\partial u} - p\frac{\partial T_A}{\partial r} + r\frac{\partial T_A}{\partial p} \\ \frac{d}{dt}\frac{\partial T_A}{\partial r} - v\frac{\partial T_A}{\partial u} + u\frac{\partial T_A}{\partial v} - q\frac{\partial T_A}{\partial p} + p\frac{\partial T_A}{\partial q} \end{bmatrix} \tag{3.10}$$

The terms from equation (3.10) are separated and grouped into inertial and Coriolis-centripetal components as shown

$$\tau_H = M_A\dot{\nu} + C_A\nu \tag{3.11}$$

The added Coriolis-centripetal matrices C_A is defined by

$$C_A = \begin{bmatrix} 0 & 0 & 0 & 0 & -a_3 & a_2 \\ 0 & 0 & 0 & a_3 & 0 & -a_1 \\ 0 & 0 & 0 & -a_2 & a_1 & 0 \\ 0 & -a_3 & a_2 & 0 & -b_3 & b_2 \\ a_3 & 0 & -a_1 & b_3 & 0 & -b_1 \\ -a_2 & a_1 & 0 & -b_2 & b_1 & 0 \end{bmatrix} \tag{3.12}$$

where

$$\begin{aligned} a_1 &= X_{\dot{u}}u + X_{\dot{v}}v + X_{\dot{w}}w + X_{\dot{p}}p + X_{\dot{q}}q + X_{\dot{r}}r \\ a_2 &= X_{\dot{v}}u + Y_{\dot{v}}v + Y_{\dot{w}}w + Y_{\dot{p}}p + Y_{\dot{q}}q + Y_{\dot{r}}r \\ a_3 &= X_{\dot{w}}u + Y_{\dot{w}}v + Z_{\dot{w}}w + Z_{\dot{p}}p + Z_{\dot{q}}q + Z_{\dot{r}}r \\ b_1 &= X_{\dot{p}}u + Y_{\dot{p}}v + Z_{\dot{p}}w + K_{\dot{p}}p + K_{\dot{q}}q + K_{\dot{r}}r \\ b_2 &= X_{\dot{q}}u + Y_{\dot{q}}v + Z_{\dot{q}}w + K_{\dot{q}}p + M_{\dot{q}}q + M_{\dot{r}}r \\ b_3 &= X_{\dot{r}}u + Y_{\dot{r}}v + Z_{\dot{r}}w + K_{\dot{r}}p + M_{\dot{r}}q + N_{\dot{r}}r \end{aligned} \tag{3.13}$$

The elements of M_A are estimated by numeric integration of two-dimensional added mass coefficients over the length of the body using the strip theory approach in [4]. Only the major submerged components are considered for added mass and the vehicle geometry is simplified as seen in Figure 3.2. We compute the 2D added mass coefficients of the strut, fore wing, and aft foils by approximating its cross sectional shape as an elliptical or a rectangular strip with mean chord length and constant height as shown in Figure 3.3. A_{11} , A_{22} , A_{33} indicates 2D added mass coefficients for flow in x, y, and z axis respectively and ρ is the water

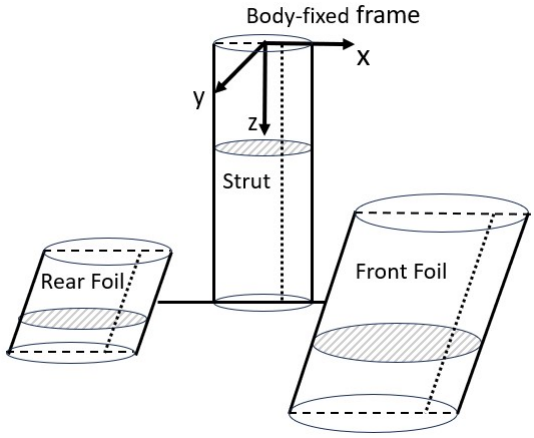

Figure 3.2: Simplified submerged geometry for added mass approximation

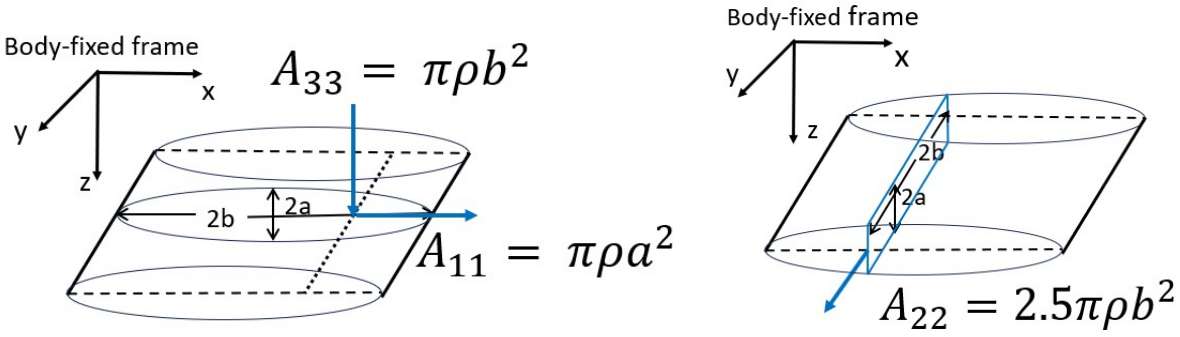

(a) Simplification for x or z axis flow

(b) Simplification for y axis flow

Figure 3.3: Assumed hydrofoil geometry with formula for two-dimensional hydrodynamic added mass coefficients

density. The diagonal components of the vehicle added mass matrix M_A are calculated by the following formula

$$\begin{aligned}
X_{\dot{u}} &= \int_{-S_F/2}^{S_F/2} A_{11_F} dy + \int_{-S_R/2}^{S_R/2} A_{11_R} dy + \int_0^{S_S} A_{11_S} dz \\
Y_{\dot{v}} &= \int_0^{C_F} A_{22_F} dx + \int_0^{C_R} A_{22_R} dx + \int_0^{S_S} A_{22_S} dz \\
Z_{\dot{w}} &= \int_{-S_F/2}^{S_F/2} A_{33_F} dy + \int_{-S_R/2}^{S_R/2} A_{33_R} dy + \int_0^{C_S} A_{33_S} dx \\
K_{\dot{p}} &= \int_{-S_F/2}^{S_F/2} y^2 A_{33_F} dy + \int_{-S_R/2}^{S_R/2} y^2 A_{33_R} dy + \int_0^{S_S} z^2 A_{22_S} dz \\
M_{\dot{q}} &= \int_{-S_F/2}^{S_F/2} x_F^2 A_{33_F} dy + \int_{-S_R/2}^{S_R/2} x_R^2 A_{33_R} dy + \int_0^{S_S} z^2 A_{11_S} dz \\
N_{\dot{r}} &= \int_{-S_F/2}^{S_F/2} y^2 A_{11_F} dy + \int_{-S_R/2}^{S_R/2} y^2 A_{11_R} dy + \int_0^{S_S} x_S^2 A_{22_S} dz
\end{aligned} \tag{3.14}$$

where S denotes the wing span, C is the chord length, x_F, x_R and x_S are the x coordinates of the quarterchord for the front, rear, and strut foils. The subscripts $_F$, $_R$, and $_S$ refer to the front foil, rear foil and the strut respectively. Because of the thin front, rear, and strut foil sections, we assume that the contribution of A_{22_F}, A_{22_R}, and A_{33_S} in calculating $K_{\dot{p}}$, $M_{\dot{q}}$, and $N_{\dot{r}}$ are negligible. Additionally, we assume that the moment contribution of the ellipsoidal cross section occurs at the quarter chord which is a good approximation for the location of the lift and drag force vector for a foil. Due to the geometrical symmetry in xz plane, the off-diagonal coefficients $X_{\dot{v}}$, $X_{\dot{p}}$, $X_{\dot{r}}$, $Y_{\dot{w}}$, $Y_{\dot{q}}$, $Z_{\dot{p}}$, $Z_{\dot{r}}$, $Z_{\dot{q}}$, and $N_{\dot{r}}$ and their symmetric counterparts are negligible and taken to be zero. Furthermore, since the hydrofoils were simplified as elliptical strips, $X_{\dot{w}}$ and $K_{\dot{r}}$ are also taken to be zero, leaving only $X_{\dot{q}} = M_{\dot{u}}$,

$Y_{\dot{p}} = K_{\dot{v}}$, $Y_{\dot{r}} = N_{\dot{v}}$, $Z_{\dot{q}} = M_{\dot{w}}$ as non-zero off-diagonal coefficients which are calculated as

$$\begin{aligned}
X_{\dot{q}} &= \int_{-S_F/2}^{S_F/2} z_F A_{11_F} dy + \int_{-S_R/2}^{S_R/2} z_R A_{11_R} dy + \int_0^{S_S} z A_{11_S} dz \\
Y_{\dot{p}} &= -\int_0^{C_F} z_F A_{22_F} dx - \int_0^{C_R} z_R A_{22_R} dx - \int_0^{S_S} z A_{22_S} dz \\
Y_{\dot{r}} &= \int_{x_F - \frac{3C_F}{4}}^{x_F + \frac{C_F}{4}} x A_{22_F} dx + \int_{x_R - \frac{3C_R}{4}}^{x_R + \frac{C_R}{4}} x A_{22_R} dx + \int_0^{S_S} x_S A_{22_S} dz \\
Z_{\dot{q}} &= -\int_{-S_F/2}^{S_F/2} x A_{33_F} dy - \int_{-S_R/2}^{S_R/2} x A_{33_R} dy - \int_0^{C_S} x_S A_{33_S} dx
\end{aligned} \tag{3.15}$$

where z_F and z_R are the z coordinates of the quarterchord for the fore and aft foil. The signs in calculating the off-diagonal coefficients reflect how M_A is referenced in Equation 3.4. For example, positive acceleration in pitch induces negative resistive force in x axis, but since M_A is on the left hand side of the equation, $X_{\dot{q}}$ is a positive term.

3.4 Restoring Forces and Moments

In hydrodynamics, restoring forces refer to the gravitational and buoyancy forces of the vehicle. As stated when M_{RB}, was defined, the measured mass of the vehicle is 47.9 kg. To approximate the buoyant force, we use the simplified CAD model to measure the total volume as well as the volumetric center of the fore foil, aft foil, and the strut. Note that the three component volumes were assumed to be watertight, and were defined with the same density so that the CoG of the CAD model is coincident with the volumetric center. The calculated submerged volume is 0.0080 m^3, which equates to 78 N of buoyancy, and the CoB is located at [0.069 m, 0 m, 0.661 m] in body-fixed coordinates. Both buoyancy and CoB are considered to be constant because the change in displaced volume due to the narrow mast is negligible, and we are primarily interested in conditions at which the propeller and both fore

and aft foils are fully submerged. Because the restoring forces act in Z axis of the inertial frame, they must be transformed into the body-fixed reference frame before use in Equation 3.4. Using the invertible rotation matrix J_1 defined in Equation 3.1, the restoring forces and moments vector G in body-fixed frame is expressed as

$$G_1 = J_1^{-1}(\eta_2)\begin{bmatrix} 0 \\ 0 \\ mg - \rho g V \end{bmatrix} = \begin{bmatrix} (mg - \rho g V)\sin\theta \\ -(mg - \rho g V)\cos\theta\sin\phi \\ -(mg - \rho g V)\cos\theta\cos\phi \end{bmatrix}$$

$$G_2 = \begin{bmatrix} -(mg\,y_G - \rho g V\,y_B)\cos\theta\cos\phi + (mg\,x_G - \rho g V\,x_B)\cos\theta\sin\phi \\ (mg\,x_G - \rho g V\,x_B)\cos\theta\cos\phi + (mg\,z_G - \rho g V\,z_B)\sin\theta \\ -(mg\,x_G - \rho g V\,x_B)\cos\theta\sin\phi + (mg\,y_G - \rho g V\,y_B)\sin\theta \end{bmatrix} \tag{3.16}$$

$$G = \begin{bmatrix} G_1 \\ G_2 \end{bmatrix}$$

where g is the acceleration of gravity, ρ is the water density, V is the submerged volume, and x_B, y_B and z_B are the body-fixed coordinates of the CoB.

3.5 External Forces and Moments

The external forces and moments represented by τ are comprised of the thrust and drag from the propulsor, and lift and drag forces from the mast, front wing, rear wing with elevator flaps, and rudder fin. The coefficient of drag (CoD) for the propulsor housing shown in Figure 3.4 are 0.2, 1.0, and 1.0 along the body-fixed x, y, and z axis, respectively. CoD were estimated based on the drag curve for a round-nosed cylinder with length over diameter ratio of $L/d = 4.7$ and Reynolds number of $Re \approx 2.66 \times 10^5$ at 4 m/s [6]. Assuming the drag

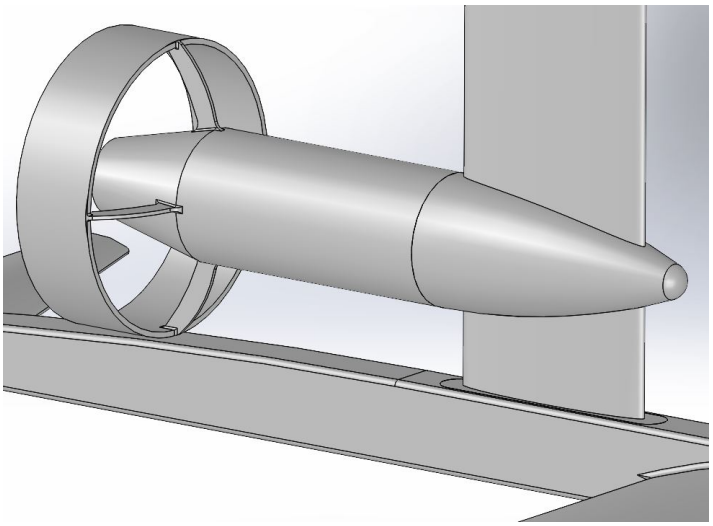

Figure 3.4: Approximated model of integrated propulsor motor housing

forces act on the centroid of the motor housing given by body-fixed coordinates $[t_x, t_y, t_z]$, the forces and the corresponding moment on the propulsor are expressed as

$$\begin{aligned} Drag_{propulsor} &= \begin{bmatrix} \frac{1}{2}\rho A_x C_{d_x}(u + q\,t_z + r\,t_y)^2 \\ \frac{1}{2}\rho A_y C_{d_y}(v - p\,t_z + r\,t_x)^2 \\ \frac{1}{2}\rho A_z C_{d_z}(w + p\,t_y - q\,t_x)^2 \end{bmatrix} = \begin{bmatrix} D_{x_p} \\ D_{y_p} \\ D_{z_p} \end{bmatrix} \\ Moment_{propulsor} &= \begin{bmatrix} t_y\,D_{z_p} - t_z\,D_{y_p} \\ -t_x\,D_{z_p} + t_z\,D_{x_p} \\ t_x\,D_{y_p} - t_y\,D_{x_p} \end{bmatrix} \end{aligned} \tag{3.17}$$

where A_x, A_y, and A_z are the reference surface area in x, y, and z axis respectively, and C_{d_x} and $C_{y_x} = C_{d_z}$ are the propulsor CoD in x, y, and z axis respectively. The propeller thrust is modeled as the difference in upstream and downstream dynamic pressure of the propeller using

$$T_{propeller} = \frac{1}{2}\rho\pi r^2(V_e^2 - V_o^2) \tag{3.18}$$

where $r = 0.0725$ m is the propeller radius, ρ is water density, V_e is exit flow velocity, and V_o is the inflow velocity. The exit velocity of the propulsor is estimated to be 6.118 m/s

based on an initial thrust measurement of 309 N at 0 m/s inflow. $T_{propeller}$ is presumed to act only in the body-fixed x axis with corresponding pitch moment $T_{propeller}\, p_z$ where p_z is the z coordinate of the propeller's axis of rotation.

The lift and drag forces of the foil components are calculated using lifting line theory, specifically the vortex lattice model described in chapter 12 of Plotkin [9]. The numerical model divides the wing span into N number of equal segments with circulation distribution and trailing vortices as indicated in Figure 3.5. The general idea of the model is to solve the

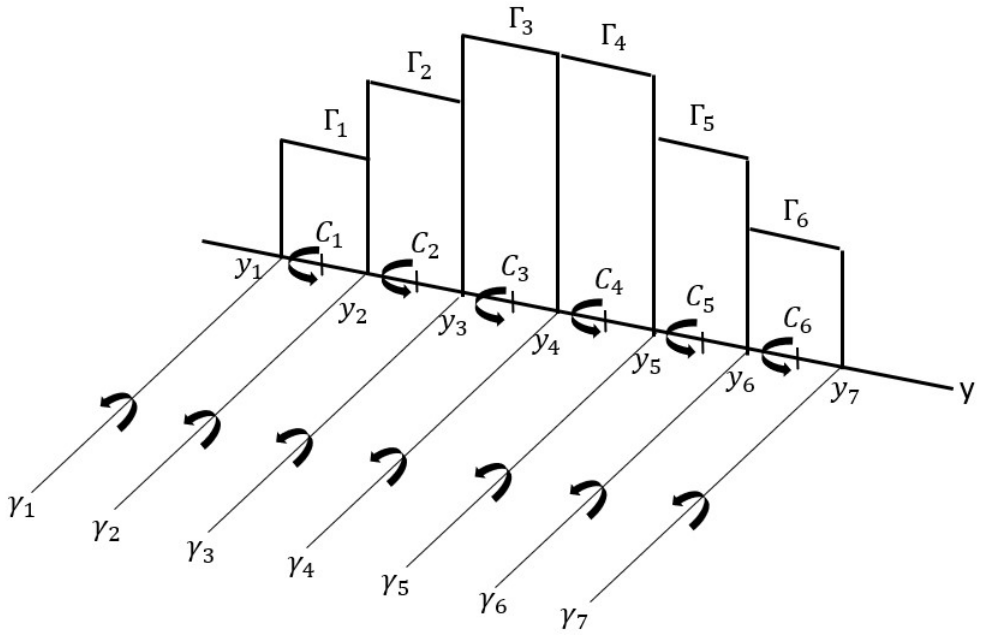

Figure 3.5: Example lifting line diagram with distribution of circulation Γ at segment centers $C_1 ... C_6$ and trailing vortex γ at segment bounds $y_1 ... y_7$

linear system of equations relating circulation at each segment center to the local lift force which is given by the equation

$$\Gamma_i = \frac{L_i}{\rho\, V_{\infty_i}} \tag{3.19}$$

where Γ is the circulation, L is the lift force, and V_∞ is the inflow velocity for $i = 1...N$. Note that the inflow velocity is adjusted based on the angular rates and the body-fixed

coordinates of quarterchord at each i-th section along the span. For example, V_{∞_i} for each front foil segment is

$$V_{\infty_i} = \sqrt{(u + q\, z_F - r\, C_i)^2 + (w + p\, C_i - q\, x_i)^2} \tag{3.20}$$

where C_i is the body-fixed y coordinates of the segment center, and x_i and z_F are the x and z coordinates of the front foil quarterchord. The segment quarterchord x_i is defined using the coordinate of the wing root quarterchord x_r and wing sweep angle δ

$$x_i = x_r - |C_i| tan(\delta) \tag{3.21}$$

The lift force at each segment is given by

$$L_i = \frac{1}{2}\rho V_{\infty_i}^2\, c_i\, l\, C_{L_i} \tag{3.22}$$

where c is the chord length, l is the length of each segment section, and C_L is the CoL. The chord distribution is defined using the tapered ratio λ

$$\begin{gathered} c_i = \frac{2\,S}{(1+\lambda)b}\left(\frac{(1-\lambda)|2\,C_i|}{b}\right) \\ \text{for} \quad \lambda = \frac{c_t}{c_r} \quad \text{and} \quad S = \frac{(c_r + c_t)b}{2} \end{gathered} \tag{3.23}$$

where b is the wing span, c_t is the chord length at wing tip, and c_r is the root chord length. The expression for sectional C_{L_i} contains the induced velocity w_i caused by the trailing vortices at the boundary of each segment where

$$\begin{gathered} C_{L_i} = C_{L0} + 2\pi\alpha_e = C_{L0} + 2\pi(\alpha_{\infty_i} - \alpha_i) \\ \alpha_i = \arctan\frac{w_i}{V_{\infty_i}} \approx \frac{w_i}{V_{\infty_i}} \end{gathered} \tag{3.24}$$

in which the effective angle of attack α_e is the difference between the inflow angle α_∞ and the induced angle α_i in radians, and C_{L0} is the known coefficient of lift (CoL) at zero angle of attack. Because the surge velocity u is often much grater than the induced velocity w_i, the small angle approximation is used for α_i. A graphical representation of the foil sectional lift and drag is shown in Figure 3.6. w_i at each segment center is the sum of the velocity

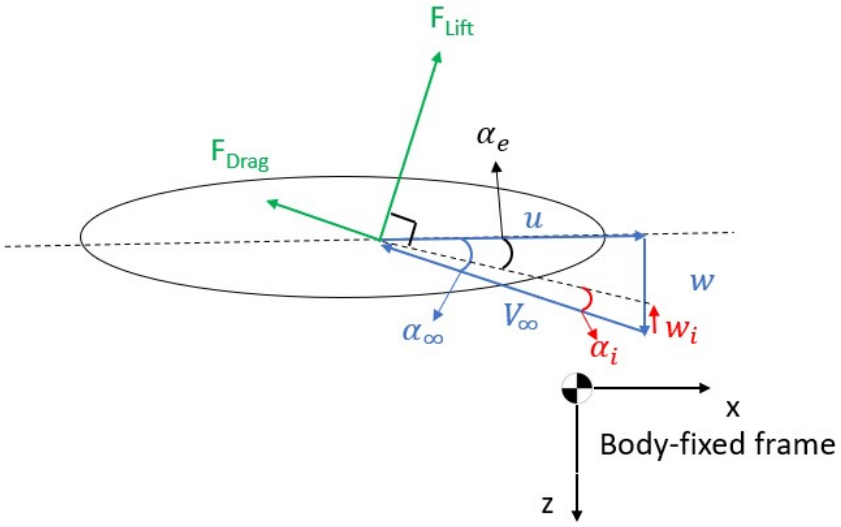

Figure 3.6: Example lift, drag, and velocity vectors for foil cross section

induced by each shed vortex γ_j at the bounds y_j for $j = 1 \dots N+1$ and is defined by

$$w_i = \sum_{j=1}^{N+1} \frac{\gamma_j}{4\pi(C_i - y_j)} = \sum_{j=1}^{N+1} \frac{\Gamma_{j-1} - \Gamma_j}{4\pi(C_i - y_j)} = \sum_{j=1}^{N} \Gamma_j \left[\frac{1}{4\pi(C_i - y_{j+1})} - \frac{1}{4\pi(C_i - y_j)} \right] \tag{3.25}$$

Defining $A_{i,j} = \frac{1}{4\pi(C_i - y_{j+1})} - \frac{1}{4\pi(C_i - y_j)}$ and substituting equation 3.25, 3.24, and 3.22 into

equation 3.19 yields

$$\begin{aligned}\Gamma_i &= \frac{1}{\rho V_{\infty_i}}\left[\frac{1}{2}\rho V_{\infty_i}^2 c_i\big(C_{L0} + 2\pi(\alpha_{\infty_i} - \frac{\sum_{j=1}^{N}\Gamma_j A_{i,j}}{V_{\infty_i}})\big)\right] \\ \Gamma_i &= \frac{V_{\infty_i}c_i}{2}C_{L0} + \pi V_{\infty_i}c_i\alpha_{\infty_i} - \pi c_i\sum_{j=1}^{N}\Gamma_j A_{i,j} \\ \Gamma_i &+ \pi c_i\sum_{j=1}^{N}\Gamma_j A_{i,j} = \frac{V_{\infty_i}c_i}{2}C_{L0} + \pi V_{\infty_i}c_i\alpha_{\infty_i}\end{aligned} \tag{3.26}$$

Equation 3.26 can then be expressed in matrix form as

$$\left(I_{N\times N} + \pi\begin{bmatrix} c_1\,A_{1,1} & \dots & c_1\,A_{1,N} \\ \vdots & \ddots & \vdots \\ c_N\,A_{N,1} & \dots & c_N\,A_{N,N}\end{bmatrix}\right)\begin{bmatrix}\Gamma_1 \\ \vdots \\ \Gamma_N\end{bmatrix} = \begin{bmatrix}\big(C_{L0} + 2\pi\alpha_{\infty_1}\big)\frac{V_{\infty_1}c_1}{2} \\ \vdots \\ \big(C_{L0} + 2\pi\alpha_{\infty_N}\big)\frac{V_{\infty_N}c_N}{2}\end{bmatrix} \tag{3.27}$$

where $I_{N\times N}$ is a N by N identity matrix. The circulation at the segment centers $[\Gamma_1 \dots \Gamma_N]^T$ can then be solved by multiplying the inverse of the left hand side matrix by the right hand side vector. The total lift force is then given by the sum

$$L = \rho\, l\sum_{i=1}^{N} V_{\infty_i}\Gamma_i \tag{3.28}$$

Assuming that the vehicle is under forward motion ($u \geq 0$), the pitch angle is $-90° < \theta < 90°$, and that the lift force at each segment acts perpendicular to α_e, the lift forces and moments broken down to body-fixed xyz components for the front or rear wing are

$$\begin{bmatrix}F_x \\ F_y \\ F_z \\ M_x \\ M_y \\ M_z\end{bmatrix} = \begin{bmatrix}\sum_{i=1}^{N} L_i \sin\alpha_{e_i} \\ 0 \\ -\sum_{i=1}^{N} L_i \cos\alpha_{e_i} \\ -\sum_{i=1}^{N} C_i L_i \cos\alpha_{e_i} \\ \sum_{i=1}^{N} x_i L_i \cos\alpha_{e_i} + z_r\sum_{i=1}^{N} L_i \sin\alpha_{e_i} \\ \sum_{i=1}^{N} C_i L_i \sin\alpha_{e_i}\end{bmatrix} \tag{3.29}$$

where z_r is the body-fixed z coordinate of the root quarterchord. For the strut, the lift force acts in the xy plane and is defined by

$$\begin{bmatrix} F_x \\ F_y \\ F_z \\ M_x \\ M_y \\ M_z \end{bmatrix} = \begin{bmatrix} \sum_{i=1}^{N} L_i \sin \alpha_{e_i} \\ -\sum_{i=1}^{N} L_i \cos \alpha_{e_i} \\ 0 \\ \sum_{i=1}^{N} C_i L_i \cos \alpha_{e_i} \\ \sum_{i=1}^{N} C_i L_i \sin \alpha_{e_i} \\ -x_r \sum_{i=1}^{N} L_i \cos \alpha_{e_i} \end{bmatrix} \tag{3.30}$$

The drag force for each segment is approximated as

$$D_i = \frac{1}{2} \rho \, l \, C_D \, c_i \, V_{\infty_i}^2 \tag{3.31}$$

where C_D is the foil CoD which is taken to be constant for moderate angles of attack before stall occurs. The drag force at each segment acts parallel to α_∞, and the drag forces and moments for front or rear wings are defined by

$$\begin{bmatrix} F_x \\ F_y \\ F_z \\ M_x \\ M_y \\ M_z \end{bmatrix} = \begin{bmatrix} -\sum_{i=1}^{N} D_i \cos \alpha_\infty \\ 0 \\ -\sum_{i=1}^{N} D_i \sin \alpha_\infty \\ -\sum_{i=1}^{N} C_i D_i \sin \alpha_\infty \\ -z_r \sum_{i=1}^{N} D_i \cos \alpha_\infty + \sum_{i=1}^{N} x_i D_i \sin \alpha_\infty \\ -\sum_{i=1}^{N} C_i D_i \cos \alpha_\infty \end{bmatrix} \tag{3.32}$$

The drag forces and moments for the strut is expressed as

$$\begin{bmatrix} F_x \\ F_y \\ F_z \\ M_x \\ M_y \\ M_z \end{bmatrix} = \begin{bmatrix} -\sum_{i=1}^{N} D_i \cos\alpha_\infty \\ -\sum_{i=1}^{N} D_i \sin\alpha_\infty \\ 0 \\ \sum_{i=1}^{N} C_i D_i \sin\alpha_\infty \\ -\sum_{i=1}^{N} C_i D_i \cos\alpha_\infty \\ -\sum_{i=1}^{N} x_i D_i \sin\alpha_\infty \end{bmatrix} \tag{3.33}$$

To define the user inputs C_{L0} and C_D to the lifting line method, the fore, aft, and strut hydrofoil cross-sections were approximated based on a rough measurement of the root chord foil geometry as an accurate CAD model was not available due to the proprietary nature of the commercial craft. Due to the thin complex profile of the front and rear wings, We make the assumption that the cross sectional profile at the wing root is kept constant throughout the wing span with varying chord length that reflect the trapezoidal foil shape. The root chord control points are then loaded into XFOIL, a subsonic airfoil design software, to estimate the C_{L0} and C_D. An example of the thin front wing cross section in XFOIL is illustrated in Figure 3.7. Solving for C_L and C_D at 0° angle of attack with Reynolds number

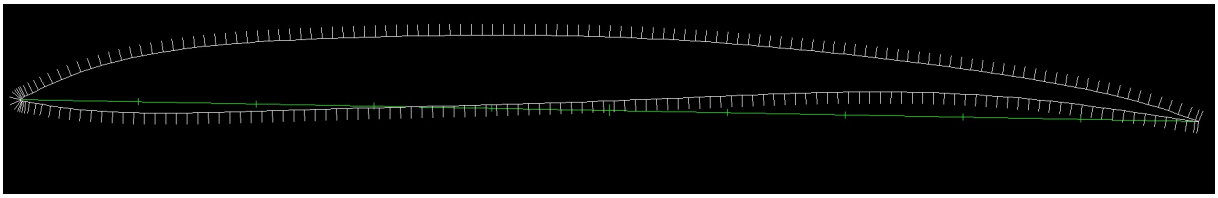

Figure 3.7: Measured front foil cross section illustrated in XFOIL

ranging from $4.08 \times 10^5 \sim 1.02 \times 10^6$ depending on the chord length at 4 m/s resulted in C_{L0} of 0.6, 0.3, and 0.0 and C_D of 0.01, 0.006, and 0.01 for front, rear, and strut foils respectively. The rudder fin has a symmetric profile of a NACA 0009 airfoil with CoD of 0.005 and C_{L0} of 0 [8]. The CoL for the stern wing is further modified by the commanded elevator flap angle which then shifts the value of C_{L0} as illustrated in Figure 3.8. A plain flap works by effectively

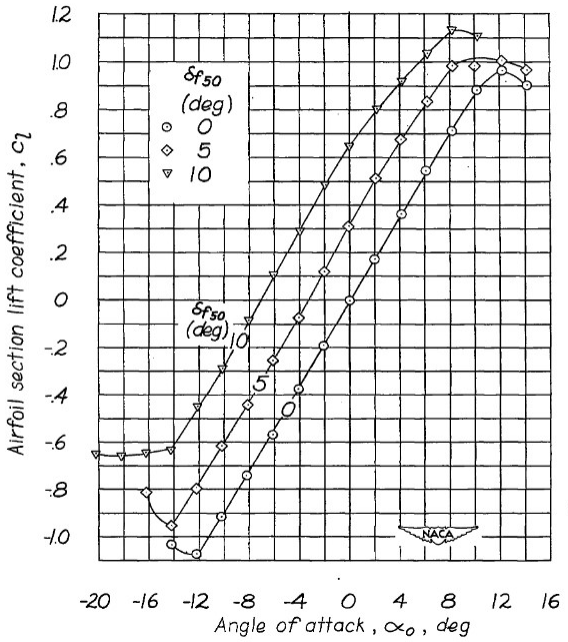

Figure 3.8: Section lift coefficient of NACA 0009 airfoil with 0.5 chord length plain flap and 0.005 chord length gap[19]

changing the camber of the wing. In doing so, the foil's angle of attack vs lift curve shifts up or down while maintaining the same shape, changing only the 0° intercept point C_{L0}. The increase in C_{L0} for the stern wing elevator flaps is approximated to be 0.04 per one degree of positive flap angle based on the experimental trends shown by Spearman [19]. The rotation direction of the elevator flaps follow the right hand rule convention around body-fixed y axis while the rudder fin follows the body-fixed z axis. Since the current implementation of the lifting line code does not account for nonlinearity of C_L near stall, a maximum sectional lift coefficient of 1.4 is imposed for all airfoil components.

Chapter 4

Tow Tank Test

4.1 Tow Tank Experimental Setup

The mast assembly was tested at the Virginia Tech tow tank as shown in Figure 4.1. The

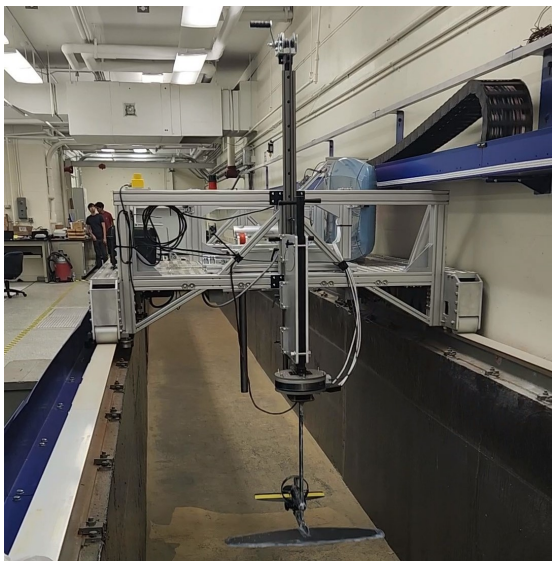

Figure 4.1: Virginia Tech's high speed tow tank carriage with hydrofoil test fixture

tow basin is 98 feet long, 6 feet wide, and 4 feet deep with a maximum carriage speed of 7 m/s. For all test runs, the desired carriage velocity, acceleration, and jerk were specified, and the measured carriage velocity and position were recorded at 50 Hz. The water temperature remained around 18.5°C, meaning that the water density likely did not change. Sufficient time is allotted at the end of each run to allow the resulting wake to dissipate and the water

surface to settle.

A custom test stand supporting the mast assembly and a six-component load cell was mounted to the tow carriage as shown in Figure 4.2. The load cell can concurrently measure

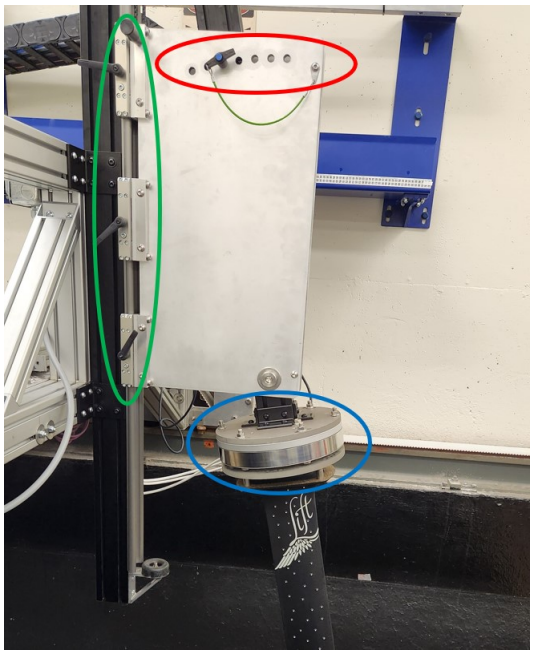

Figure 4.2: Towing tank test stand with pitch angle adjustment circled in red, linear rail circled in green and load cell circled in blue. The six yaw adjustment bolts are located at the top of the load cell.

all xyz forces and moments, and is calibrated with a decoupling matrix to minimize crosstalk between each axes. The center of the load cell and its orientation is aligned with the body-fixed frame meaning that the recorded forces and moments can be directly compared to the first principles model. To induce different angles of attack, the mast assembly is rotated relative to the towing carriage axis using preset pitch adjustment holes. The submerged depth of the model is adjusted using the locking linear rails of the test rig. Additionally, different bolt patterns to mount the load cell to the test fixture allows one to set the yaw angle of the mast at 0, 5, or -7.5 degrees. Before each run, the load cell is zeroed and set to record at 100 Hz while the elevator, rudder, and throttle servos are actuated to hold a

set angle. All trial conditions were tested twice to check for reasonable repeatability in the data. The typical range of forces and moments between the two repeated runs was around 2% of the averaged value. All reported forces and moments in Section V are the means of the two runs.

4.2 Tow Tank Results

Tow tank experiments were conducted around carriage velocity of 4 m/s at maximum throttle to characterize the effect of the propulsor, pitch angle, elevator, rudder, and yaw angle on the overall body-fixed forces and moments. The nominal operating condition of 4 m/s and full throttle input were selected from prior experiences of operating the eFoil.

The forces generated by the propeller at 0 carriage speed were measured to serve as a baseline when determining the effect of inflow velocity on thrust. The resulting body-fixed forces and moments at maximum commanded rpm are shown in Table 4.1. Apart from the measured thrust in x axis, the small forces along the y and z axes suggest that a slight misalignment exists between the load cell and the mast assembly. This skewness could be due to the manufacturing tolerances in the mast's countersink holes that align the mounting bolts to the sensor. We assume that the values apart from F_x and M_y in Table 4.1 are mainly attributed to the mast misalignment and are subtracted from all full throttle load cell data in order to separate the effect of an off-centre propulsor from hydrofoil lift and drag.

Table 4.1: Measured body-fixed frame forces and moments for propulsor at max rpm and 0 m/s forward velocity

Propeller RPM	**Fx (N)**	**Fy (N)**	**Fz (N)**	**Mx (Nm)**	**My (Nm)**	**Mz (N)**
3600	319.6	27.2	-8.8	-7.2	219.4	-4.0

*Results are rounded to nearest tenth based on load cell resolution

Multiple tests were carried out at different tow speeds and pitch angles, with full throttle input, and zero throttle with the propeller completely removed. The differences in the measured forces with and without the propeller can then be used to observe the thrust at varying inflow speed and the effect of the propeller flow on overall lift. During the tests, the rudder and elevator angles were set to 0 degrees with the mast submerged at 50 cm, which is roughly two thirds of the strut length. Four carriage speeds and six pitch angles were tested. The trial conditions are summarized in Table 4.2.

Table 4.2: Overview of different pitch angle and speed conditions tested with propulsor at full and zero throttle

Speed (m/s)	**Pitch Angle (deg)**					
	0°	**2.5°**	**5°**	**7.5°**	**10°**	**12.5°**
3.5	T	T	T	T	T	T
4	T / N	T / N	T / N	T / N	T	T
4.5	T	T	T	T	T	T
5	T / N	T / N	T / N	T / N	T	T

T = Full Throttle, N = No Throttle

An example of the measurements acquired for a given run is shown in Figure 4.3. We can observe that all forces and moments start to settle to a steady-state value soon after the carriage reaches the target speed of 4 m/s. The load cell measurements then hold steady for roughly 2 seconds until the time at which the carriage begins to decelerate. The lack of large fluctuations in forces and moments during the steady-state window as well as good alignment between measured forces and moments and the measured carriage velocity gives us confidence that the mast assembly achieved a stable steady-state condition without excessive unwanted disturbances. The load cell forces and moments are averaged within this steady-state interval and used for comparison in the following analyses.

Using the measured forces F_x and F_z for 4 m/s and 5 m/s at 0°, 2.5°, 5°, and 7.5° pitch, the

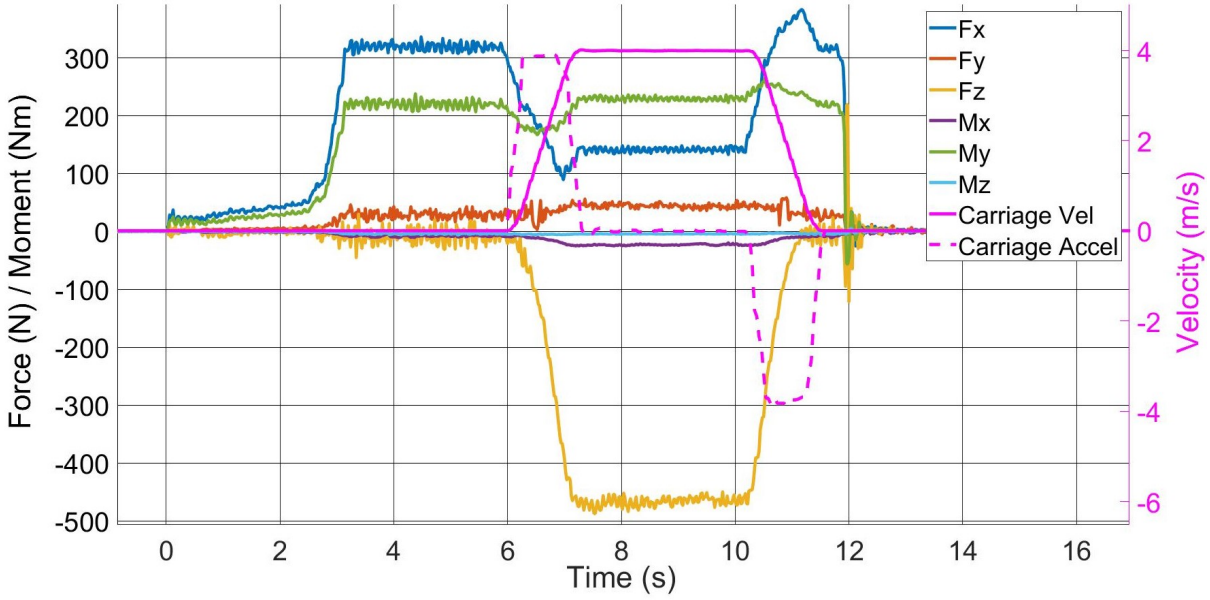

Figure 4.3: Time aligned six-component sensor and tow carriage data at 4 m/s and 0° pitch angle. The maximum throttle input is commanded before launching the towing carriage.

lift of the mast assembly with and without the propeller were compared. We assume that the difference in F_x between full and no throttle trials is solely due to the propeller thrust T. We further assume that a portion of the measured F_z in the max throttle run is due to the mast misalignment rather than lift. Therefore, the z axis force measured in the stationary propeller test in Table 4.1 is subtracted from the F_z taken at a nonzero carriage speed with full throttle. Since the sensor is aligned with the body-fixed frame, both components of F_x and F_z at pitch angle θ is taken into account when calculating the drag and lift which act

in relation to the carriage velocity axis. An example calculation for the case of 4 m/s is

$$\begin{aligned} F_D^{[\mathrm{NT}]} &= \cos\theta F_x^{[\mathrm{NT}]} + \sin\theta F_z^{[\mathrm{NT}]} \\ F_L^{[\mathrm{NT}]} &= -\sin\theta F_x^{[\mathrm{NT}]} + \cos\theta F_z^{[\mathrm{NT}]} \\ T_x &= F_x{}^{[\mathrm{FT}]} - F_x{}^{[\mathrm{NT}]} \\ T_z &= \frac{T_x^{[\mathrm{FT}]}}{F_x{}^{[0]}} F_z{}^{[0]} \\ F_D^{[\mathrm{FT}]} &= \cos\theta(F_x^{[\mathrm{FT}]} - T_x) + \sin\theta(F_z^{[\mathrm{FT}]} - T_z) \\ F_L^{[FT]} &= -\sin\theta(F_x^{[\mathrm{FT}]} - T_x) + \cos\theta(F_z^{[FT]} - T_z) \end{aligned} \tag{4.1}$$

where $^{[FT]}$ and $^{[NT]}$ indicate measurement at full and no throttle conditions, respectively, and $^{[0]}$ refers to the stationary propulsor test in Table 4.1. Comparison of the lift forces with and without the propeller are shown in Table 4.3. The propeller flow seems to induce a small increase in lift which could be due to the propulsor speeding up the flow on the upper surface of the hydrofoils. The difference, however, is small enough to use full throttle data to approximate the overall lift characteristics of the mast assembly.

Table 4.3: Increase in total lift force at varying speed and pitch angle due to the effect of the propulsor at max and zero throttle

Speed (m/s) / Pitch (deg)	**Lift (N) Full Throttle**	**Lift (N) No Throttle**	**Relative Increase (%)**
4 / 0°	-590.1	-573.4	2.91
4 / 2.5°	-920.3	-892.3	3.14
4 / 5°	-1247.7	-1210.0	3.12
4 / 7.5°	-1545.5	-1511.8	2.23
5 / 0°	-981.8	-969.1	1.32
5 / 2.5°	-1532.1	-1504.3	1.85
5 / 5°	-2075.9	-2047.0	1.41
5 / 7.5°	-2553.2	-2530.5	0.90

Ideally, the drag of the mast assembly would be obtained from the test runs without the propeller, but due to limited time allocation of the tow tank facility, tests at 3.5 and 4.5 m/s were unable to be carried out. The drag at those speeds is estimated from the full throttle trials by subtracting the estimated reduced thrust. Under the assumption that the motor controller is maintaining the commanded 3600 RPM regardless of carriage speed or pitch angle, we first obtain the reduced thrust force at 4 m/s and 5 m/s by observing the difference in measured x axis force with and without the propeller. By plotting the change in thrust with carriage velocity shown in Figure 4.4, we can obtain a 2nd order best fit line that roughly represents the nonlinear reduction in propeller thrust with increased inflow speed. Although the thrust seems to slightly decrease with higher pitch angle, we do not account

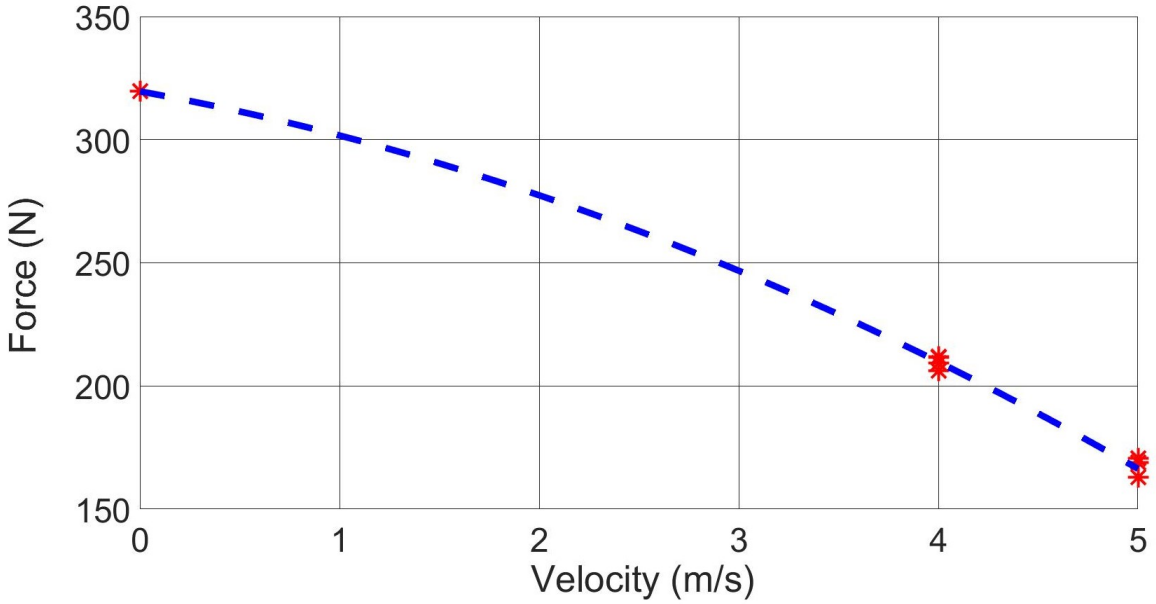

Figure 4.4: Measured thrust at maximum propeller RPM with best-fit line describing decrease in thrust with increasing inflow speed.

for this small effect in estimating propeller force at different inflow speeds.

Using the predicted thrust at 3.5 m/s and 4.5 m/s, we can obtain the lift and drag forces from the full throttle trial runs by carrying out the same calculations in (4.1). The lift and

drag curve with respect to pitch or angle of attack for this case is shown in Figure 4.5 and Figure 4.6. Note that the lift stays roughly linear until around 7.5 degrees where it begins to decline, likely due to stall on the main and stern hydrofoils. Overall, the general trend of both the lift and drag curves with increasing angle of attack agrees with expectations. The increase in lift and drag with higher carriage speed is also consistent with the squared velocity term that appears in the fundamental lift and drag equations.

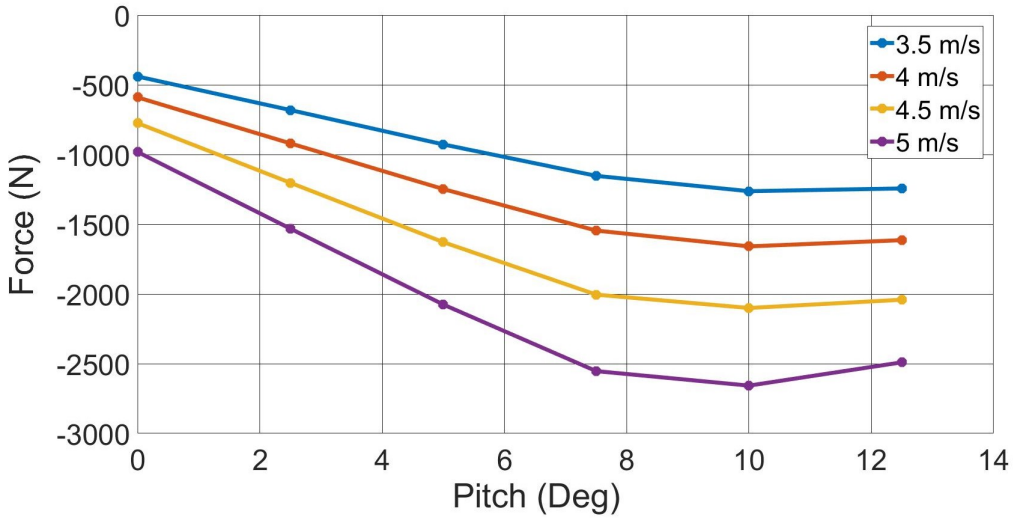

Figure 4.5: Increase in lift with larger angle of attack for the mast assembly at four different forward velocities.

Tests at 4 and 4.5 m/s with 5 degree pitch angle, 50 cm of submergence, and varying elevator flap angle from -20 to 20 degrees were conducted to determine the effect of the elevator flaps on the total lift and pitch moment. Pitch angle of 5° was specifically chosen because it corresponds to 1250 N of lift at 4 m/s, which is just enough to support the 47.5 kg liftboard with 80 kg payload out of the water. We note that lift at this operating condition is consistent with supporting a human user, which the eFoil was originally designed to achieve. Positive elevator angle indicates rotation around body-fixed $+y$ axis for both port and starboard flaps. The resultant lift and pitch moment are shown in Figure 4.7 and Figure 4.8. We can

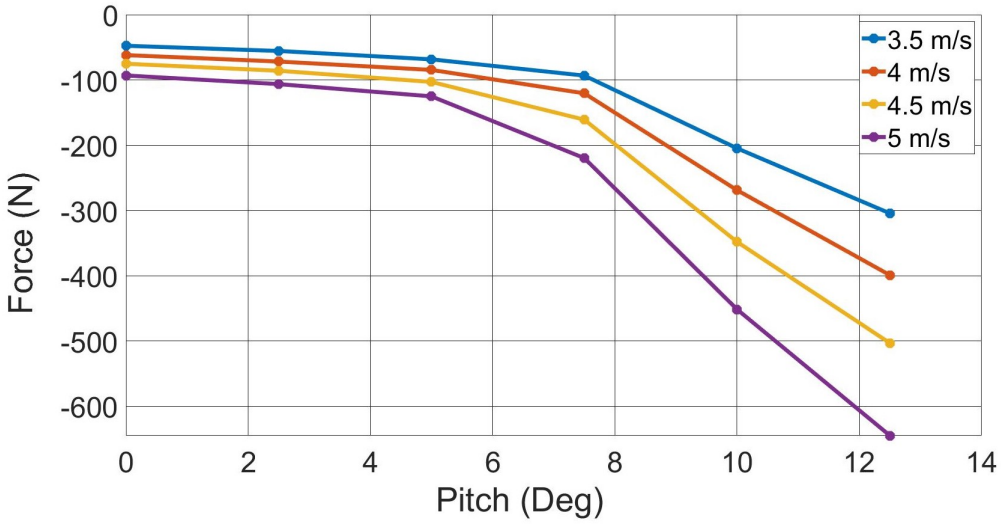

Figure 4.6: Increase in drag with larger angle of attack for the mast assembly at four forward velocities.

observe the effect of the elevator flaps modifying the effective angle of attack from the set 5° pitch angle of the stern foil. The linear behavior of the lift force suggest that even at max flap angle, the effective angle of attack on the rear wing did not shift enough to reach stall. Once again, the difference between the two curves at 4 and 4.5 m/s are proportional to squared velocity as expected.

Experiments at 4 m/s at 5 degree pitch angle, 50 cm of submergence, and varying rudder flap angle from -15 to 15 degrees were conducted to determine the effect of the rudder flap on roll moment. The results are shown in Figure 4.9. Positive rudder angle indicates flap rotation around body-fixed $-z$ axis. The rudder fin offered maximum roll moment correction of +4.3 Nm to -7.4 Nm.

Alternative way to generate roll moment is by commanding the port and starboard elevator flaps to rotate in opposing direction. Results at 4 m/s, 5° pitch angle, 50 cm of submergence, and varying split flap angles from -20 to 20 degrees are shown in Figure 4.10. Positive 10° split angle denotes +10° rotation of port flap and -10° rotation of starboard flap about the

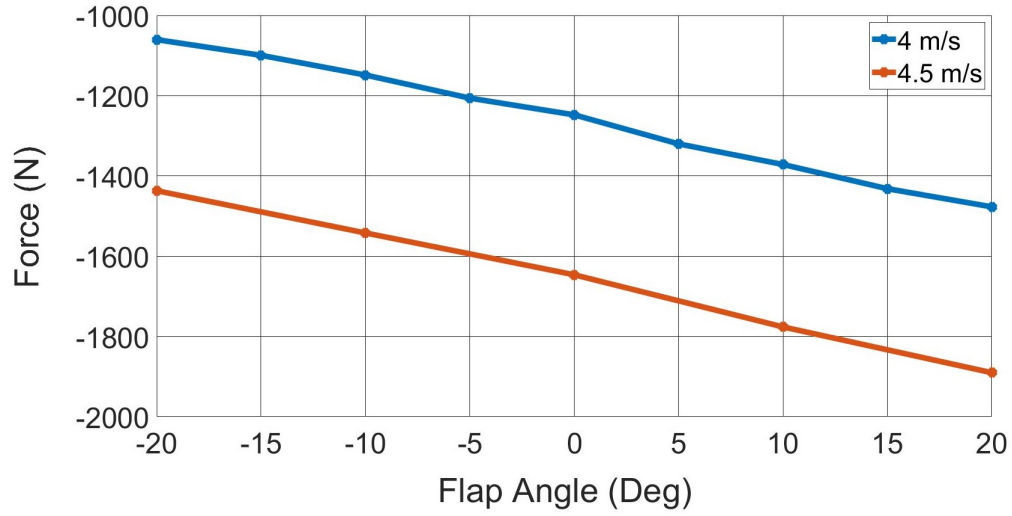

Figure 4.7: Increase in lift force with increasing elevator flap angle at two forward velocities.

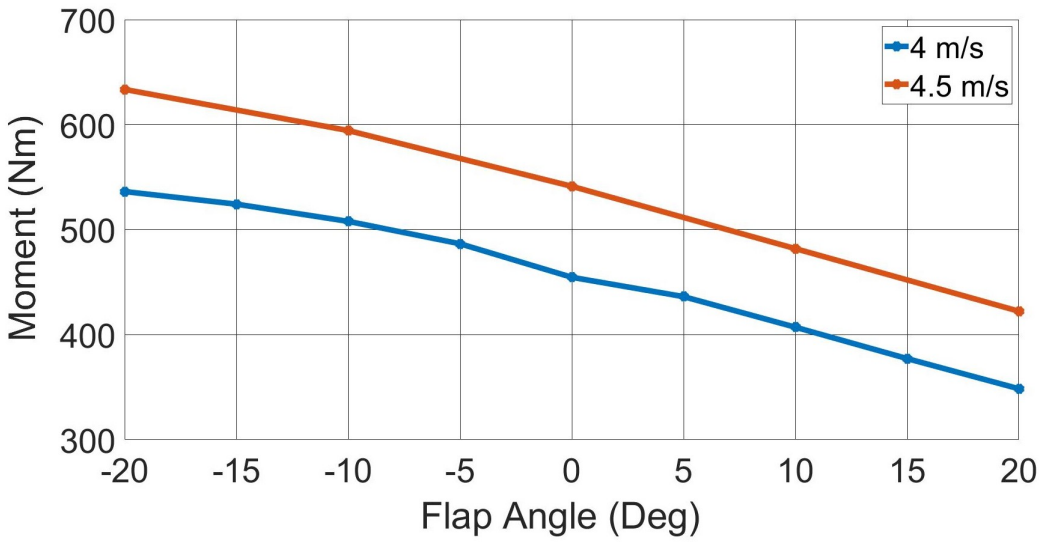

Figure 4.8: Decrease in body-fixed y axis pitch moment with increasing elevator flap angle at two forward velocities.

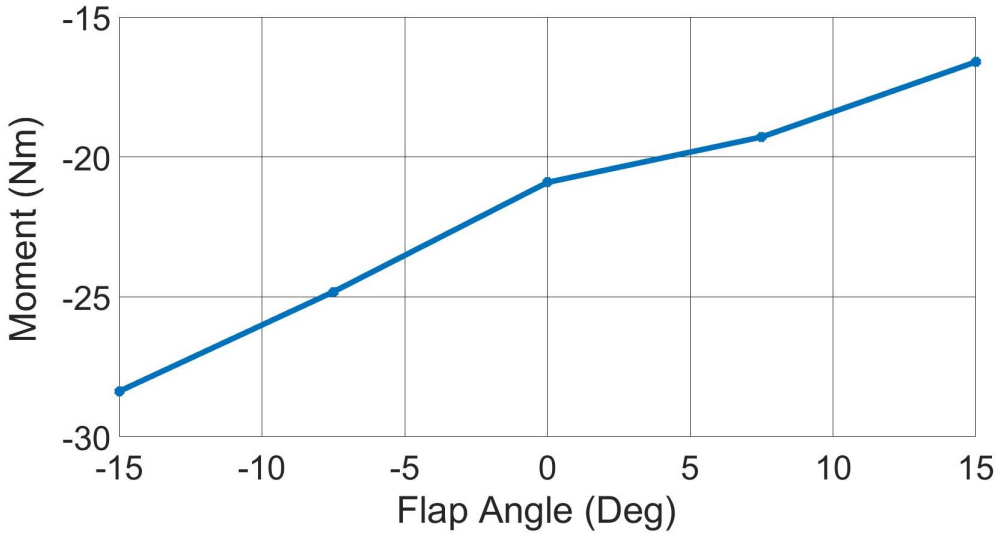

Figure 4.9: Body-fixed x axis roll moment at varying rudder flap angle with 4 m/s forward velocity.

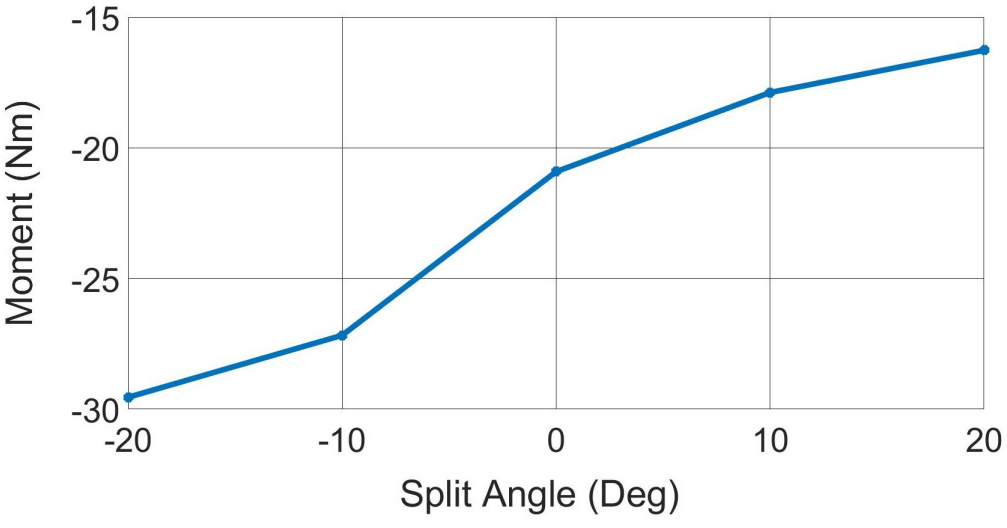

Figure 4.10: Body-fixed x axis roll moment at different split elevator angle with 4 m/s forward velocity.

body-fixed $+y$ axis. This configuration offered similar amount of roll adjustment as the rudder with +4.7 Nm to -8.6 Nm of added moment.

Trials at varying carriage speed with 0° pitch angle and 50 cm of submergence were carried out to verify the effect of yaw angle on the mast assembly. Because the yaw imposes angle of attack on the vertical strut, we are primarily interested in the y axis body frame force and the roll moment presented in Figure 4.11 and Figure 4.12. The slope of F_y stays roughly

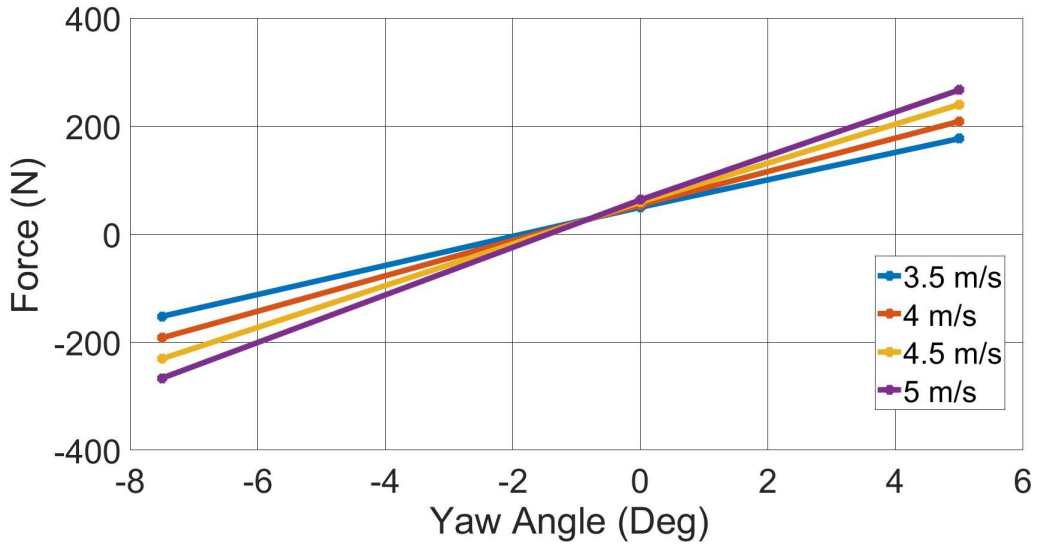

Figure 4.11: Body-fixed y axis force with varying yaw angle at four forward speeds.

the same between the two yaw angles in accordance to the expected linear increase in lift of the vertical strut with angle of attack. It also indicates that the strut has not reached the stall angle even at 7.5° of yaw. Furthermore, the large roll moment gives an estimate of how much additional roll control is needed in order to turn the vehicle at constant yaw angle.

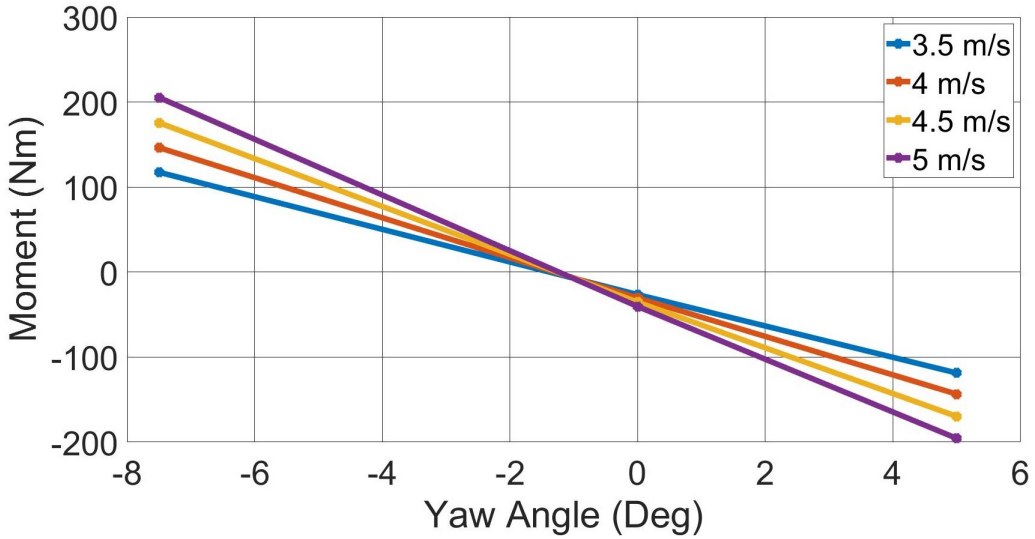

Figure 4.12: Body-fixed x axis roll moment with varying yaw angle at four forward speeds

4.3 Comparison of Dynamic Model Prediction and Experimental Results

We compare the steady-state vehicle trends measured with the tow tank experiments to the predicted values from the first principles model. These effects include the propeller thrust, total lift of the mast assembly, the change in lift with elevator flaps, the roll control moment of the rudder or split flaps, and the side force generated with yaw angle. Because the load cell sensor is zeroed before each trial run, the effect of weight and buoyancy is ignored. Since the tow tank measurements are analyzed at steady-state, the hydrodynamic added mass terms are disregarded.

The differences in thrust of the simplified propeller model and the measured tow tank values are illustrated in Table 4.4. The first principles model under-predicts the propulsor force by 16% at 4m/s and 39% at 5 m/s. The prediction does not seem to sufficiently capture the complexity in propeller thrust reduction especially at higher speeds, which depend on

Table 4.4: Measured and predicted thrust at maximum propeller rpm for different inflow velocities

	Inflow Velocity (m/s)		
	0	**4**	**5**
Measured Thrust (N)	319.6	211.6	168.9
Predicted Thrust (N)	309	176.9	102.6

multitude of factors ranging from and not limited to blade pitch, diameter, duct shape, number of blades and RPM that were not accounted for in Equation (4).

The predicted and measured lift of the mast assembly at nominal operating speed of 4 m/s is shown in Figure 4.13. It is apparent that the the stall angle assumption using the fore and

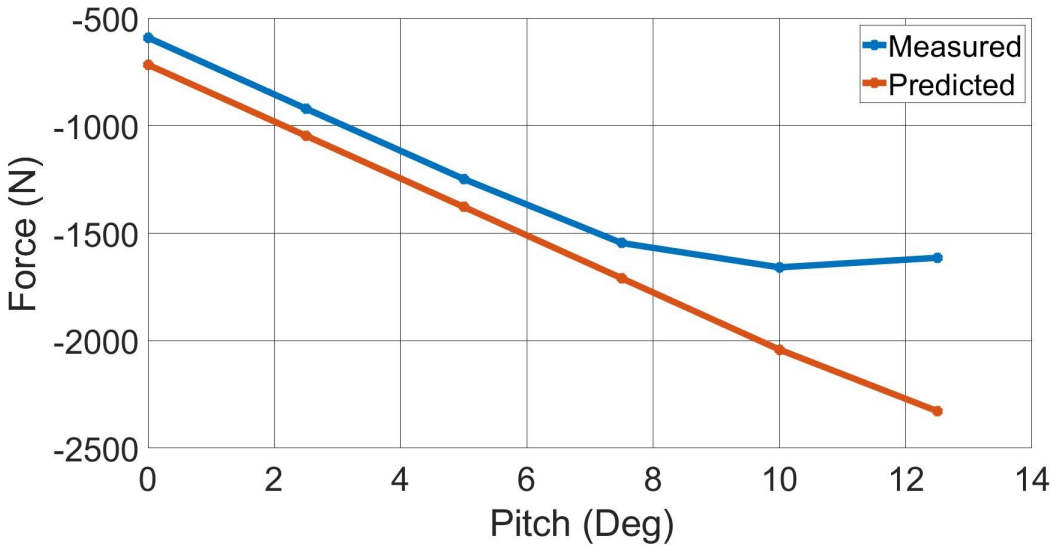

Figure 4.13: Measured and predicted lift with increasing angle of attack at 4 m/s carriage velocity and 50 cm submergence.

aft wing root chord geometry in the first principles model overestimates the actual critical angle of attack. Even in the linear region, the predicted lift overshoots the measured values by 10 to 21%. A plausible cause for the error, among other contributing modeling errors, is the geometry of the relatively thin cambered hydrofoils with span-wise curvature which is

difficult to accurately measure and approximate.

The estimated increase in lift with elevator flap angle is presented in Figure 4.14. The lift

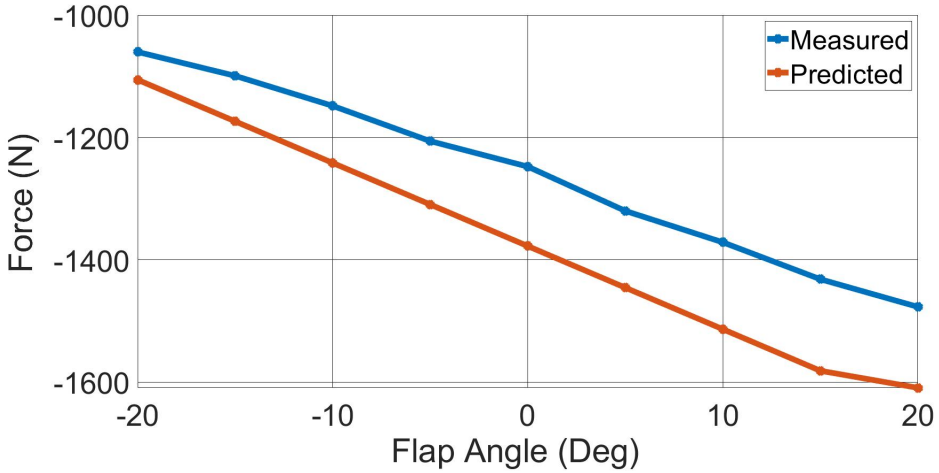

Figure 4.14: Measured and predicted lift with increasing elevator flap angle at 4 m/s carriage velocity and 50 cm submergence.

effects of the flaps in the first principles model are 4% to 10% greater than the measured force in the tow tank. The slope of the predicted curve is also steeper than the experimental trend. In fact, the model anticipates the effective angle of attack of the stern wing to increase to the point of stall at around 15° elevator angle. The discrepancy in the first principle model is attributed to the lack of a general formula in predicting the amount for which a plain flap alters the value of C_L for a wing. This value seems to commonly be defined with experiments [19] rather than calculated, making it difficult to estimate for use in a dynamic model.

The moment from rudder or split flap angle generated by the first principle model is displayed in Table 4.5. The estimated roll moment contribution of both the rudder and split flaps were much larger than the measured data. This could be due to a number of factors that the 6DoF model does not consider such as the possible interaction of the propeller located just in front of the rudder, the flow interruption caused by the flap control linkages, and physical

Table 4.5: Measured and predicted roll moment with varying rudder or split flap angle

	Rudder Angle (deg)				
	-15	**-7.5**	**0**	**7.5**	**15**
Measured Moment (Nm)	-28.4	-24.8	-20.9	-19.3	-16.6
Predicted Moment (Nm)	-14.8	-7.4	0	7.4	14.8
	Split Flap Angle (deg)				
	-20	**-10**	**0**	**10**	**20**
Measured Moment (Nm)	-29.5	-27.2	-20.9	-17.9	-16.3
Predicted Moment (Nm)	-22.4	-16.3	0	16.5	30.8

deflection of the flaps under load. Although the dynamic model has over-predicted the lift forces for the mast assembly, elevator flaps, and rudder fin, it underestimates F_y produced by the vertical strut as illustrated in Table 4.6.

Table 4.6: Measured and predicted force in body-fixed y axis with varying yaw angle

	Yaw (deg)		
	-7.5	**0**	**5**
Measured Force (N)	-192.1	54.0	208.7
Predicted Force (N)	-101.6	0	69.0

In general, the first-principles dynamic model overestimates the steady-state forces measured in the tow tank. In particular, the predicted reduction in propeller thrust with inflow speed, overall lift of the mast assembly, and the change in lift due to elevator and rudder angles were larger than their experimentally measured values. On the contrary, the calculated lift of the strut due to yaw angle is smaller in the dynamic model than the tow tank data.

Chapter 5

Height Controller

5.1 Fitting to Tow Data

Taking note of the disparities between the theoretical and experimental results outlined in Section 4.3, certain parts of the first principles dynamic model require adjustments to more accurately reflect the actual hydrofoil performance. Rather than tuning the relatively complex lifting line model described in Section 3.5, a simplified function to predict $\tau_{est} = [F'_x, F'_y, F'_z, M'_x, M'_y, M'_z]^T$ is created so that it can be easily altered to reflect the observed forces and moments at each tested condition in the tow tank. Given θ, ψ, $\dot{X}$, δ_e, δ_r which are the pitch angle, yaw angle, inertial X axis velocity, elevator flap angle, and rudder angle respectively, we define τ_{est} to represent the total applied body forces and moments that closely match the tow data.

The main components of τ_{est} were assumed to be defined by seven hydrodynamic parameters shown in Table 5.1. Note that due to its cylindrical shape, the propulsor C_D for flow in y and z axis is assumed to be the same. Since the focus is on the pitch plane motion, we assume that the yaw angle is small, and C_L for the symmetrical foils of the rudder and strut are zero. The drag of the rudder fin is not accounted in the model as it makes up for a minor portion of the overall drag.

The propulsor thrust T for different values of $\dot{X}$ is estimated using the 2nd order best fit line

Table 5.1: Hydrodynamic parameters for τ_{est}

Description	Symbol
Fore wing coefficient of lift	C_L^F
Fore wing coefficient of drag	C_D^F
Aft wing coefficient of lift	C_L^A
Aft wing coefficient of drag	C_D^A
Strut coefficient of drag	C_D^S
Propulsor coefficient of drag in x axis	$C_{D_x}^P$
Propulsor coefficient of drag in yz axis	$C_{D_{yz}}^P$

for measurements acquired from the tow test as shown in Figure 4.4. The hydrodynamic lift F_L and drag forces F_D were simply modeled with first principles as

$$\begin{aligned} F_L &= \frac{1}{2}\rho A C_L v^2 \\ F_D &= \frac{1}{2}\rho A C_D v^2 \end{aligned} \tag{5.1}$$

where ρ is the water density, A is the working foil surface area, and v is the inflow velocity. Based on the known location of each components and their hydrodynamic surface area, the idealized forces and moments from the front foil, rear foil, mast, and the propulsor can be calculated. For pitch-axis motion, we focus on F_x', F_z', and M_y' of τ_{est} which are expressed

$$\begin{aligned} F_x' = \frac{1}{2}\rho v^2 \Bigg[S_F C_F (C_L^F \sin\alpha_\infty - C_D^F \cos\alpha_\infty) + S_A C_A \Big((C_L^A + C_{L\delta}^A \delta_e) \sin\alpha_\infty - \\ (C_D^A + C_{D\delta^2}^A \delta_e^2 + C_{D\delta}^A \delta_e) \cos\alpha_\infty \Big) - (S_S + Z) C_S C_D^S \Bigg] - \frac{1}{2}\rho |u| u A_x^P C_{D_x}^P + T \end{aligned} \tag{5.2}$$

$$F'_z = \frac{1}{2}\rho v^2 \Bigg[S_F C_F(-C_L^F \cos\alpha_\infty - C_D^F \sin\alpha_\infty) + S_A C_A \Bigg(-(C_L^A + C_{L\delta}^A \delta_e)\cos\alpha_\infty - (C_D^A + C_{D\delta^2}^A \delta_e^2 + C_{D\delta}^A \delta_e)\sin\alpha_\infty \Bigg) \Bigg] - \frac{1}{2}\rho |w| w A_{yz}^P C_{D_{yz}}^P \tag{5.3}$$

$$M'_y = \frac{1}{2}\rho v^2 \Bigg[S_F C_F \Bigg(C_L^F(x_F \cos\alpha_\infty + z_F \sin\alpha_\infty) - C_D^F(x_F \cos\alpha_\infty - z_F \sin\alpha_\infty) \Bigg) + S_A C_A \Bigg((C_L^A + C_{L\delta}^A \delta_e)(x_A \cos\alpha_\infty + z_A \sin\alpha_\infty) - (C_D^A + C_{D\delta^2}^A \delta_e^2 + C_{D\delta}^A \delta_e)(x_A \cos\alpha_\infty - z_A \sin\alpha_\infty) \Bigg) - (\frac{(S_S + Z)}{2} - Z)(S_S + Z) C_S C_D^S \Bigg] - z_p \frac{1}{2}\rho |u| u A_x^P C_{D_x}^P + z_p T \tag{5.4}$$

where $S\_$ is the span, $C\_$ is the chord, α_∞ is the inflow angle, A_x^P and A_{yz}^P are the propulsor cross sectional area normal to x and y axes, $x\_$ and $z\_$ is the body frame coordinates of the wing quarterchord, z_p is the body coordinate of the propulsor center axis, and Z is the inertial frame coordinate. Subscript $_F$ indicates fore wing, $_A$ is the aft wing, $_S$ is the strut, and $_P$ is the propulsor. To account for the shift in C_L and C_D due to the elevator flap angles, the coefficients $C_{L\delta}^A, C_{D\delta^2}^A, C_{D\delta}^A$ are introduced. These values were determined from the measured τ using the method which is described at the end of Section 5.1.

The seven hydrodynamic parameters in Table 5.1 were optimized utilizing Matlab's global search solver [20] which uses the Matlab fmincon interior point algorithm [1], [2], and [21] at multiple start points generated from scatter search method [5] to find the minimum of a constrained nonlinear function. In this case, the function to minimize is the sum of normalized squared error between entries of measured τ and calculated τ_{est} that correspond to pitch-plane motion

$$\epsilon(F_x, F'_x, F_z, F'_z, M_y, M'_y) = \frac{|F_x - F'_x|^2}{|F_x|^2} + \frac{|F_z - F'_z|^2}{|F_z|^2} + \frac{|M_y - M'_y|^2}{|M_y|^2} \tag{5.5}$$

We note that the variables in (5.5) are functions of the seven hydrodynamic parameters we seek to estimate. While minimizing (5.5), we impose the constraints $-2 < C_L < 2$ and $0 < C_D < 2$.

We estimate the variables in Table 5.1 at multiple values of inflow angle α. The resulting trend for C_L and C_D when optimized over α is shown in Figure 5.1, 5.2, and 5.3. Note

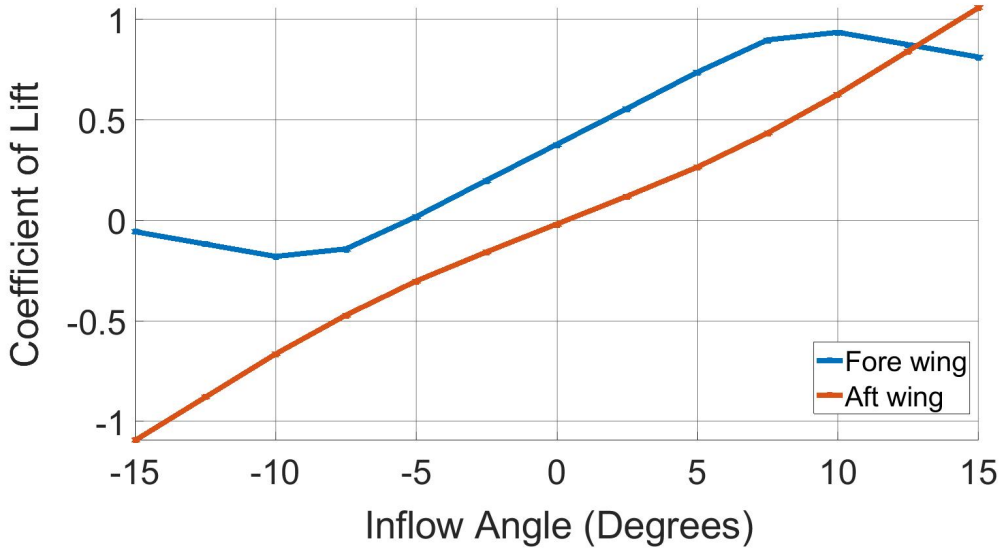

Figure 5.1: Change in predicted C_L^F and C_L^A for fore and aft foils with inflow angle

that for the tow tank tests, the value of α is the same as the pitch angle because inertial Z velocity is constrained to zero. Otherwise, the inflow angle in the pitch plane is $\alpha = \tan w/u$. We utilized the measured τ for test runs where only the pitch angles were varied from 0° to 12.5° with specified $\dot{X}$ and $\psi = \delta_e = \delta_r = 0°$. For each test run, the optimizer identifies the best C_L and C_D values that minimizes the error term in Equation 5.5. Because only the positive pitch angles could be tested in the tow tank, we assume that C_L is mirrored about the horizontal and vertical axes of the plots at the 0° pitch intercept while C_D is reflected about the vertical axis. C_L and C_D values for any pitch angles that lie between the measured runs are linearly interpolated between their two nearest points when calculating τ_{est}.

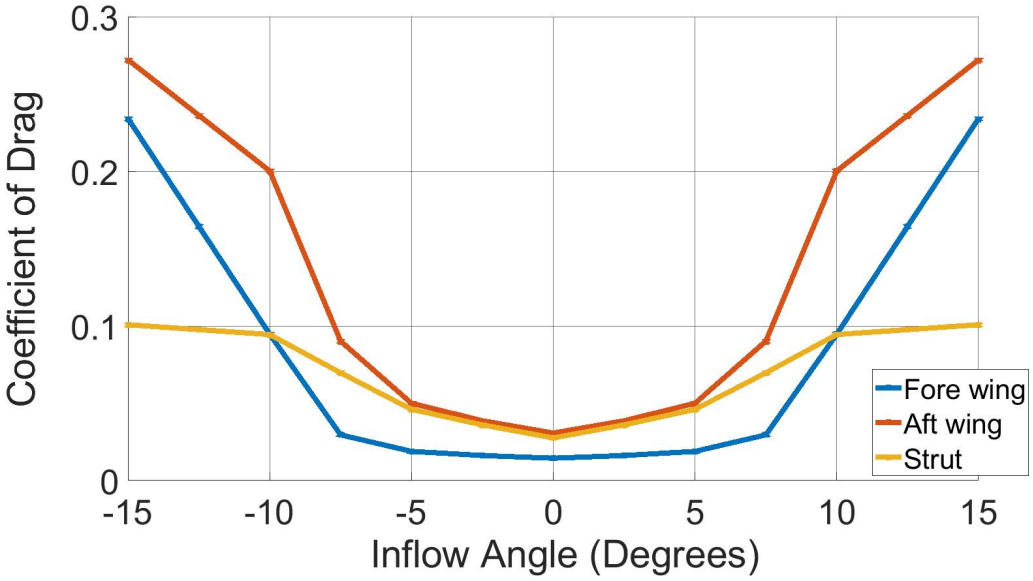

Figure 5.2: Change in predicted C_D^F,C_D^A, and C_D^S for fore, aft, and strut foils with inflow angle

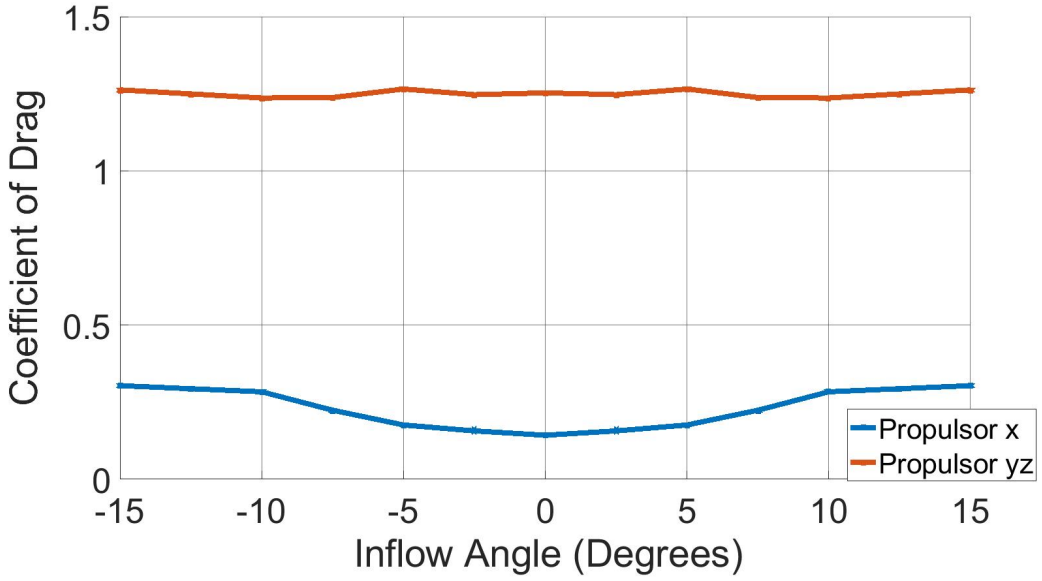

Figure 5.3: change in $C_{D_x}^P$ and $C_{D_{yz}}^P$ for propulsor in x and yz axes with inflow angle

To quantify the effect of the flap angles on aft wing coefficients C_L^A and C_D^A, we use the test data where δ_e is varied from -20° to 20° with fixed $\dot{X}$, $\theta = 5°$, and $\psi = \delta_r = 0°$. Since the elevator flap modifies the aft foil characteristics, the global search solver only estimates the rear wing C_L^A and C_D^A while the other five coefficients are held constant at the value corresponding to $\theta = 5°$ in Figure 5.1, 5.2, and 5.3. The resulting change in aft wing C_L^A and C_D^A due to elevator flap angle is shown in Figure 5.4. The change in C_L^A due to δ_e is

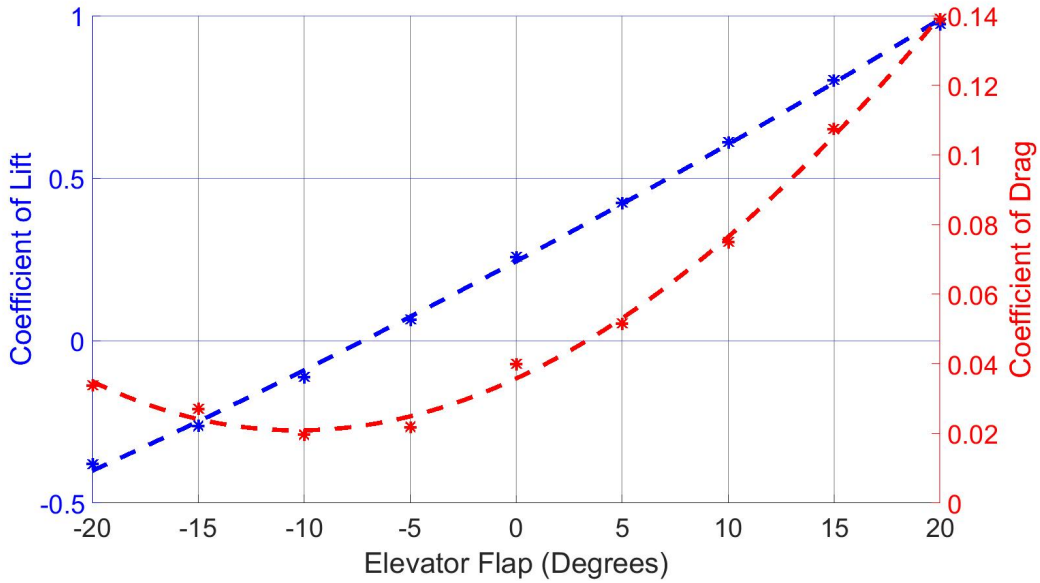

Figure 5.4: Best-fit line used to define the change in aft wing coefficients C_L^A in blue and C_D^A in red with varying flap angle.

approximated with a linear best fit curve where its slope is the $C_{L\delta}^A$ in Equation 5.2. The change in C_D^A due to δ_e is approximated with a quadratic regression where its second and first order terms are the $C_{D\delta^2}^A$ and $C_{D\delta}^A$, respectively, in Equation 5.2.

5.2 Simulated Controller

In this section, we discuss the simulated height controller model and its predicted performance. With the trend in Figure 5.1, 5.2, and 5.3 for the seven main parameters in Table 5.1 that define the applied vehicle forces and moments, we can substitute τ_{est} for τ in Equation 3.5. Since the derivatives for the vehicle states ν and η are known, an ordinary differential equation (ODE) solver can be used to numerically integrate and simulate the vehicle motion given the initial states and the commanded inputs, which is the elevator flap angle. The propeller speed is held constant at 3600 RPM. Therefore, the thrust value is solely determined from the inflow velocity. For the ODE solver, Matlab ode45 function was used which is based on explicit Runge-Kutta(4,5) formula [3], [16]. A control loop can be set up as illustrated in Figure 5.5 with a proportional outer loop for the desired and measured height and PID inner loop for the desired and measured pitch angle.

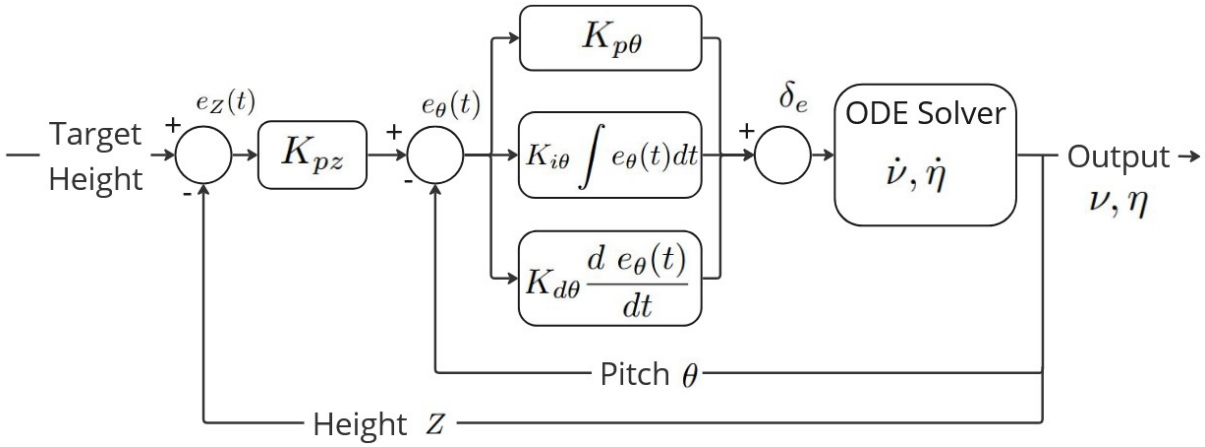

Figure 5.5: Height controller diagram with outer height loop and inner pitch loop which outputs elevator flap angle commands to the vehicle.

For preliminary field trials, a human rider was employed to operate the vehicle. The operator can take control of the vehicle when needed to steer clear of any obstacles during and at the end of each test run. Since the focus of this study is on developing a controller for pitch-axis

motion, the operator can also provide stabilizing roll moment. For each test, the role of the rider is to hold the throttle to a preset value and start the height controller once the vehicle starts planing on the water surface. The rider attempts to remain stationary and only correct for small roll motion as the height controller is turned on. The total mass, rotational inertia and center of gravity is adjusted in Equation 3.5 to account for the rider.

The goal of the controller model in Figure 5.5 is to roughly determine the control gains that can be used as a starting point when implementing the controller in the field. Following one of the many common guidelines for tuning PID gains [13] and referencing other underwater vehicle systems [14], $K_{pZ} = 0.4$, $K_{p\theta} = 4.0$, $K_{i\theta} = 0.2$, and $K_{d\theta} = 0.4$ were selected. The general idea behind the chosen gains were to have a slow height loop for gradual ascent to the target height with a fast responsive pitch loop for meeting the pitch angle commanded by the outer height loop. The value of the commanded pitch angle from the height loop is limited to be between +15° from -15° since it is well past the stall angle of around 7.5°. The output of the pitch loop is limited to +20° to -20° to reflect the limit of the flap angle actuation while the output of $K_{i\theta}$ term in the pitch loop is limited to +5° to -5°. The flap commands for the vehicle are updated at 10 Hz, and the servo slew rate is not accounted for since it is much faster than the vehicle dynamics. The predicted performance of this controller for a target height of 0.35 m at $\dot{X} = 4.6$ m/s is shown in Figure 5.6. Although the vehicle height is indicated as a positive value while the angles are shown in degrees for convenience, the actual vehicle loop follows the inertial Z axis convention and uses radians for calculating both pitch and elevator flap angles.

As the board buoyancy is not currently implemented in the model, the simulation will assume that Z can only take on value of 0 to -1 meter. Furthermore, the initial rapid change in pitch angle at the beginning of the predicted height controller performance won't reflect reality as the buoyancy of the board resists the pitch moment until the hull is sufficiently elevated

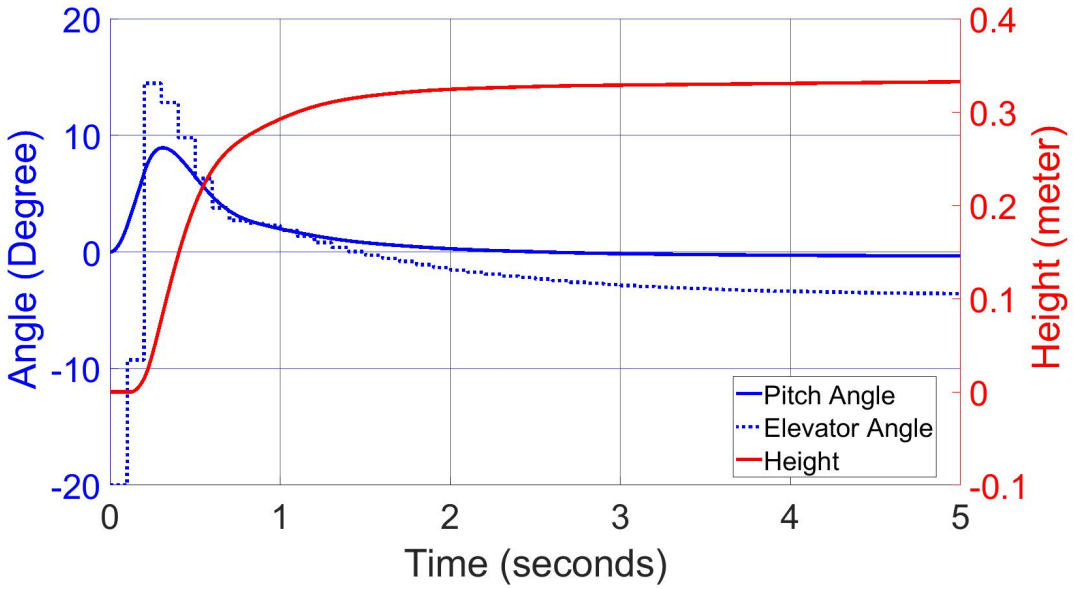

Figure 5.6: Predicted height controller performance at $\dot{X} = 4.6$ m/s and target height of 0.35 m with initial gain values: $K_{pZ} = 0.4$, $K_{p\theta} = 4.5$, $K_{i\theta} = 0.2$, and $K_{d\theta} = 0.4$. The vehicle pitch and commanded flap angle are in blue and the vehicle height is in red.

off the water surface, therefore, only the motion once the vehicle is foil-borne should be considered when comparing to the field data.

5.3 Field Trials

For this section, we present the implementation of the initial height controller as described in Section 5.2 during field trials in Claytor Lake, Virginia as well as the resulting vehicle motion measured when foiling condition was achieved. As this is an initial attempt at the vehicle height control, the focus will be on the pitch plane motion. The tests were also conducted when there were little to no wind to minimize any wave effects especially as the hull planes across the surface.

The initial gains for the height controller were tuned in the field to achieve foiling condition.

Since the simulation model did not account for the hull buoyancy that exists before the board completely leaves the water surface, the height loop did not initially command enough desired pitch to overcome the hull resistance and provide enough angle of attack on the wings as seen in Figure 5.7. Since the height loop needs to slightly overshoot the desired pitch angle at the

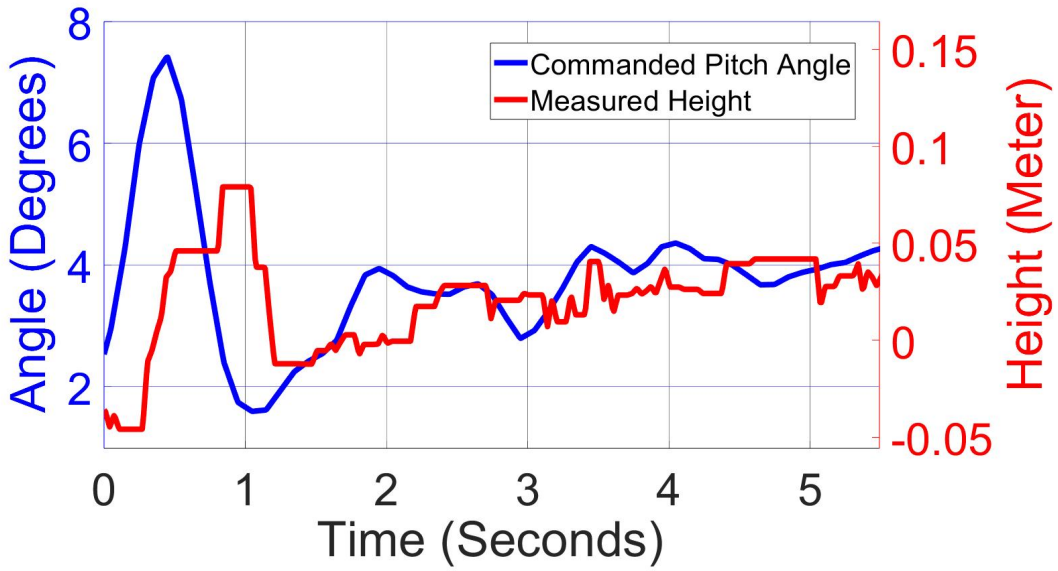

Figure 5.7: Desired pitch output from the outer height loop is in blue and measured height is in red when $K_{pZ} = 0.4$. After the initial desired $\theta \approx 7.5°$ command, the vehicle height does not continue to increase.

start to account for the board buoyancy, the K_{pZ} was increased to 0.6 from 0.4, producing the outputs in Figure 5.8 where the hull is fully lifted out of the water. Another issue that we encountered during field trials is that occasionally the vehicle would briefly pitch down soon after the target height command is sent to start the height controller. The recorded data shown in Figure 5.9 suggests that the derivative feedback was too large, which was addressed by decreasing $K_{d\theta}$ to 0.25 from 0.4. This was likely a consequence of increasing K_{pZ}. Because the outer height loop outputs an increased target pitch angle, the inner pitch loop responds by commanding greater negative elevator angle. This in turn increased the pitch rate and caused the $K_{d\theta}$ term to add too much positive flap angle at the start. Although the vehicle

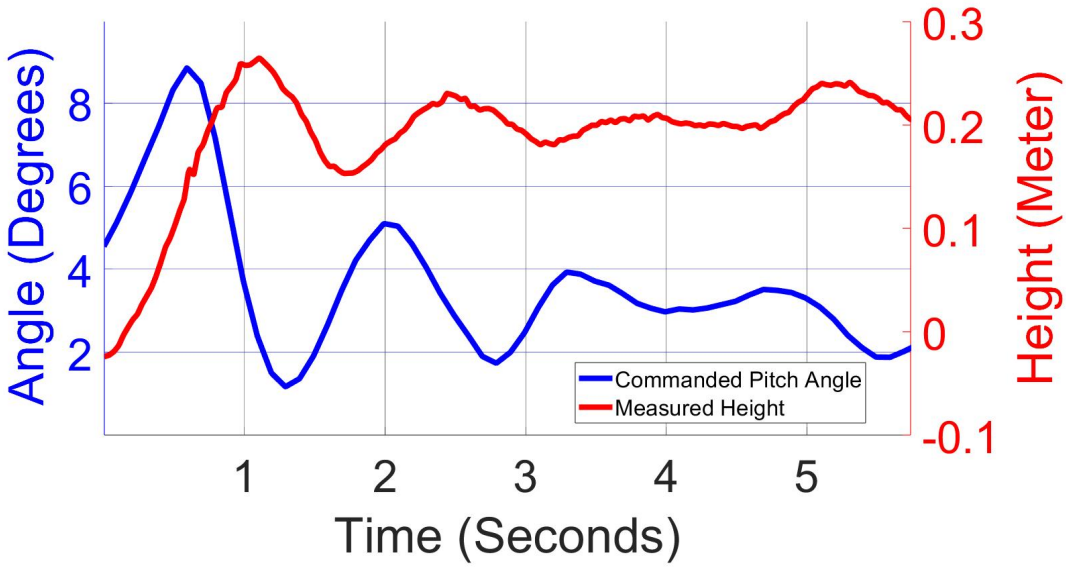

Figure 5.8: Desired pitch output from the outer height loop is in blue and measured height is in red when $K_{pZ} = 0.6$. After the initial desired $\theta \approx 8.8°$ command, the vehicle elevates off of the water surface towards the target height.

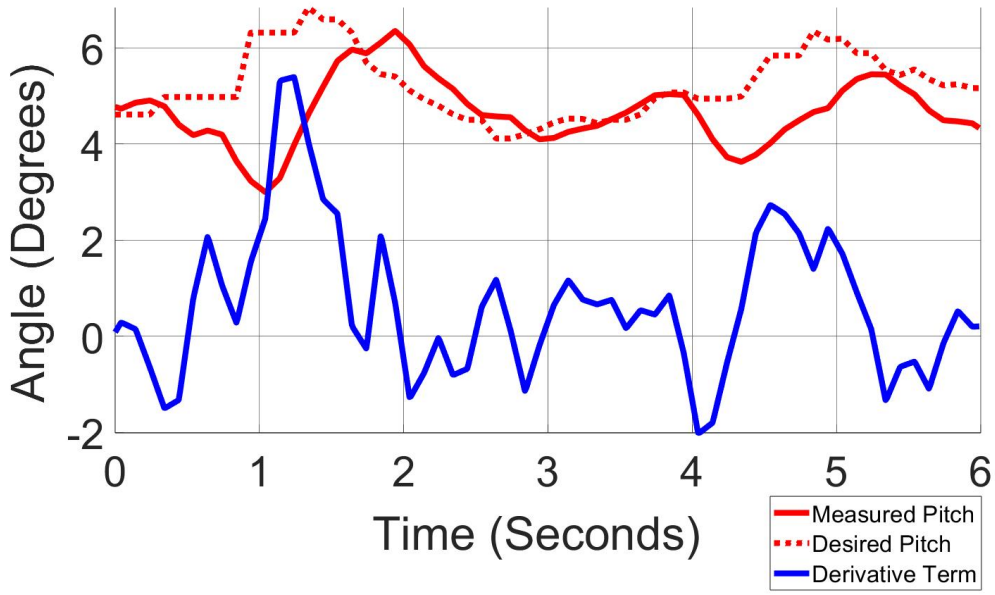

Figure 5.9: Measured vehicle pitch is in red, desired pitch is in dashed red, and $K_{d\theta}$ contribution to the elevator command output is in blue when $K_{d\theta} = 0.4$. As the outer height loop commands higher pitch angle to increase the height, $K_{d\theta}$ term adds too much commanded elevator angle to slow the pitch rate.

was unable to fully reach the target height of 0.35 m with the initial adjustment to the gain, it did achieve steady flight above the water surface. The recorded height, pitch, and elevator flap commands during one of the instances in the field is shown in Figure 5.10 To assess the

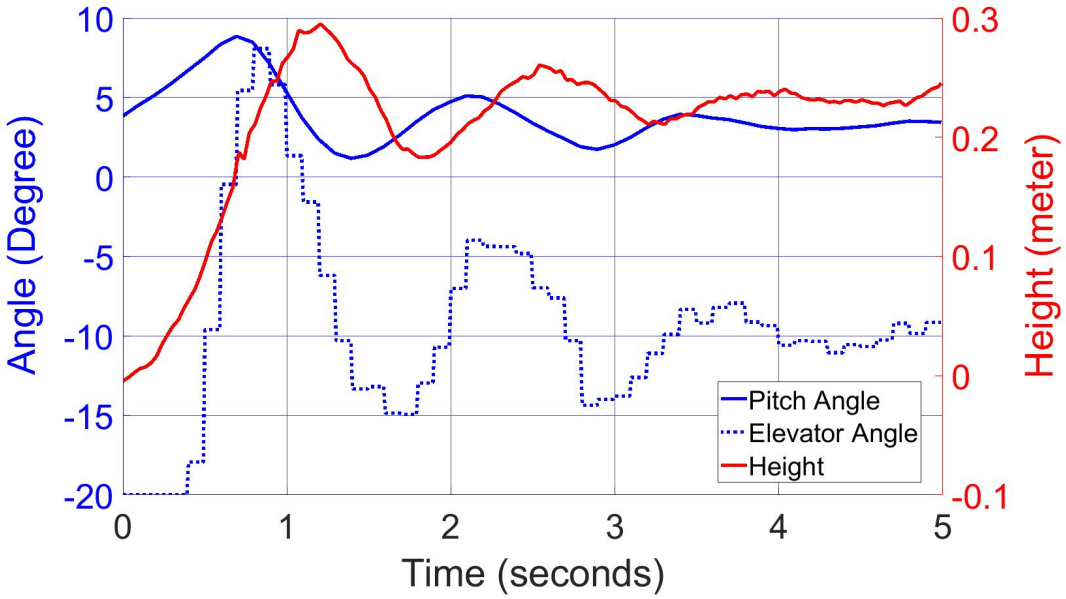

Figure 5.10: Measured height controller performance with $K_{pZ} = 0.6$, $K_{p\theta} = 4.5$, $K_{i\theta} = 0.2$, and $K_{d\theta} = 0.25$ for a target height of 0.35 m

accuracy of the dynamic model, we compare the motion of the vehicle measured during field trials with the motion predicted by the model in Figure 5.11 with the same controller gain values. The difference between the measured and the simulated pitch angle is noteworthy. In the field, θ changes noticeably slower than the simulation, and settles at a value of around 3.5° compared to the predicted 0°. A major reason for the discrepancy is that the simulation model reaches a higher steady-state surge velocity $u \approx 5.7$ m/s than what is observed in the field which is $u \approx 4.8$ m/s, explaining why a lower θ in the simulation was able to generate enough lift to maintain the vehicle foil-borne. However, the measured tow tank force F_x in the body frame x axis when the inflow velocity $v = 4.5$ m/s, is at least +110 N as shown in Figure 5.12. This F_x measured in the tow experiments does account for the simulation model accelerating to a much higher surge velocity than the field data until the increased hydrofoil

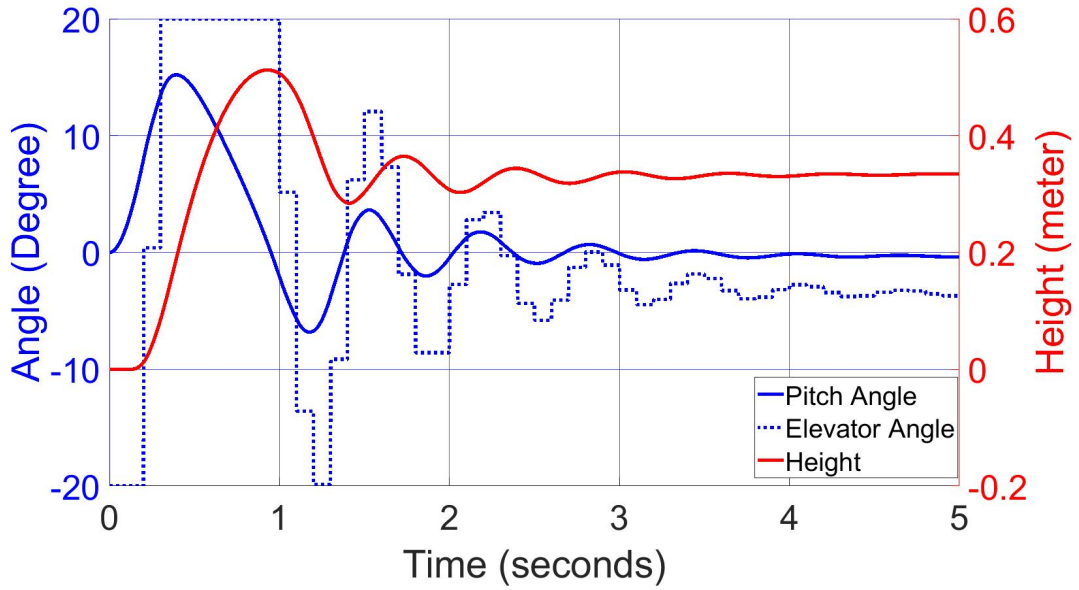

Figure 5.11: Predicted height controller performance with $K_{pZ} = 0.6$, $K_{p\theta} = 4.5$, $K_{i\theta} = 0.2$, and $K_{d\theta} = 0.25$ for a target height of 0.35 m

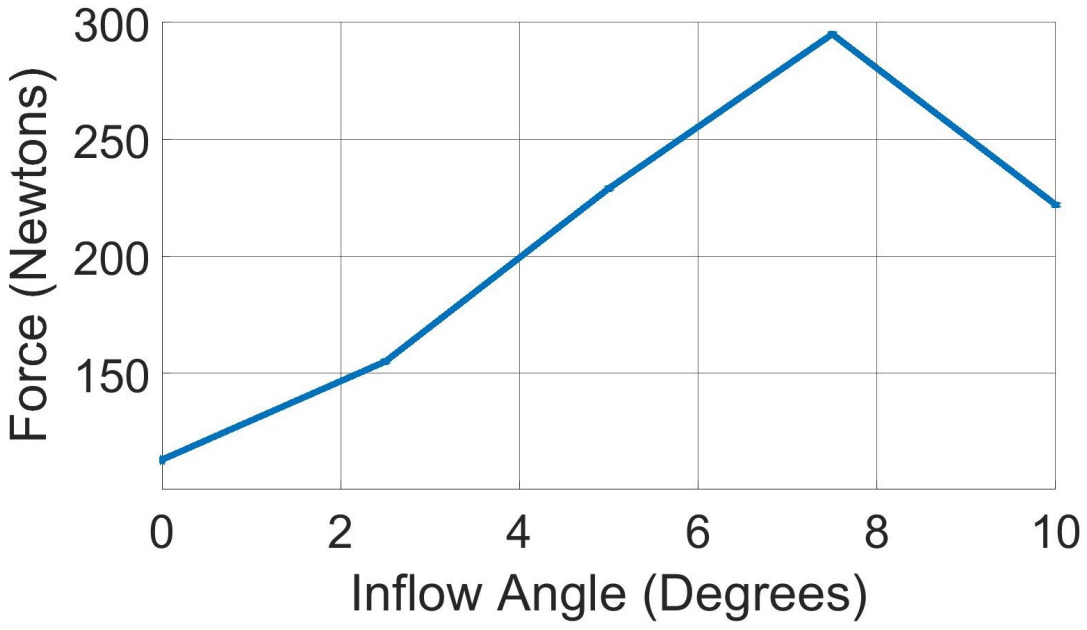

Figure 5.12: Measured force in the body frame x axis with varying pitch angles for 4.5 m/s tow carriage speed. The propulsor thrust and x axis component of the foil lift contributes to the significant F_x that leads to the higher simulated steady-state surge velocity.

drag matches the reduction in propeller thrust. This behavior likely indicates that either the propulsor behaves differently in the field than in the tow tank and produces much lower thrust or there is an unaccounted non-steady state force that was not present in the tow tank but appears in the field tests. Both cases also give some rationale for why the measured pitch motion is noticeably slower. Because apart from weight, only the hydrodynamic forces are significant on the vehicle when foiling, a reduced force in the x axis most likely indicate a smaller pitch moment as hydrodynamic forces always occur below the vehicle center of gravity.

Chapter 6

Conclusions

6.1 Conclusion and Futher Studies

In general, the first-principles dynamic model overestimates the steady-state forces measured in the tow tank. In particular, the predicted reduction in propeller thrust with inflow speed, overall lift of the mast assembly, and the change in lift due to elevator and rudder angles were larger than their experimentally measured values. On the contrary, the calculated lift of the strut due to yaw angle is smaller in the dynamic model than the tow tank data. The simplified first principle model does not seem to adequately capture the nonlinear hydrodynamic effects due to stall and possible fluid flow interaction effects between the main and aft foils.

Utilizing the measured forces and moments in the tow tank, an initial height controller for a single mast hydrofoil vehicle was simulated and implemented in the field. The mismatch between the simulated pitch motion and the slower pitch dynamics observed in the field seems to stem from significant forces during testing, where the vehicle is not at a steady-state velocity, that counteract the measured steady-state forces in the tow tank

The theoretical study is being continued, including higher fidelity methods such as potential flow methods with viscous corrections and full RANS solvers for the calculation of the steady and unsteady hydrodynamic characteristics of the 3D scanned hydrofoil assembly. We can examine the hydrodynamic contribution of each individual components and mod-

ify the dynamic model accordingly to achieve better accuracy.Further modifications to the vehicle such as sensors for static and stagnation pressure and new aft wing assembly with higher control moment and rigidity are also being implemented for improved control and measurements of the vehicle state.

Bibliography

[1] Richard H Byrd, Mary E Hribar, and Jorge Nocedal. An interior point algorithm for large-scale nonlinear programming. *SIAM Journal on Optimization*, 9(4):877–900, 1999.

[2] Richard H Byrd, Jean Charles Gilbert, and Jorge Nocedal. A trust region method based on interior point techniques for nonlinear programming. *Mathematical programming*, 89: 149–185, 2000.

[3] John R Dormand and Peter J Prince. A family of embedded runge-kutta formulae. *Journal of computational and applied mathematics*, 6(1):19–26, 1980.

[4] Thor I Fossen. *Guidance and Control of Ocean Vehicles*. John Wiley & Sons, 1994.

[5] Fred Glover. A template for scatter search and path relinking. In *European conference on artificial evolution*, pages 13–54. Springer, 1997.

[6] Sighard F Hoerner. Fluid-dynamic drag. theoretical, experimental and statistical information. *Copyright by: SF Hoerner Fluid Dynamics, Vancouver, Printed in the USA, Card Number 64-19666*, 1965.

[7] Yuh-Lin Hwang. Hydrodynamic modeling of lmrs unmanned underwater vehicle and tow tank test validation. In *Oceans 2003. Celebrating the Past... Teaming Toward the Future (IEEE Cat. No. 03CH37492)*, volume 3, pages 1425–1430. IEEE, 2003.

[8] Louis Stivers Jr. Ian H Abbott, Albert E Von Doenhoff. Summart of airfoil data. Technical report, 1945.

[9] Joseph Katz and Allen Plotkin. *Low-Speed Aerodynamics*. Cambridge Aerospace Series. Cambridge University Press, 2 edition, 2001. doi: 10.1017/CBO9780511810329.

[10] Heejip Moon, Gwyneth Steel, Hugh Dougherty, Daniel J. Stilwell, and Stefano Brizzolara. Development of a dynamic model of small autonomous hydrofoil craft. In *OCEANS 2023, Gulf Coast*, pages 1–8, 2023.

[11] Heejip Moon, Daniel J. Stilwell, and Stefano Brizzolara. Experimental study of a preliminary height controller for a small autonomous hydrofoil craft. In *15th IFAC Conference on Control Applications in Marine Systems, to appear*, 2024.

[12] Taylor Njaka, Stefano Brizzolara, and Daniel J Stilwell. Guide for cfd-informed auv maneuvering models. *Society of Naval Architects and Marine Engineers*, 2022.

[13] Katsuhiko Ogata. *Modern control engineering fifth edition*. 2010.

[14] Timothy Prestero. Development of a six-degree of freedom simulation model for the remus autonomous underwater vehicle. In *MTS/IEEE Oceans 2001. An Ocean Odyssey. Conference Proceedings (IEEE Cat. No. 01CH37295)*, volume 1, pages 450–455. IEEE, 2001.

[15] Jeonghwa Seo, Hoe-Seong Jeong, Shin Hyung Rhee, and Kyogun Chang. Towing tank model tests for propulsive performance analysis of a waterjet-propelled amphibious vehicle. *Journal of Ship Research*, 66(01):91–107, 2022.

[16] Lawrence F Shampine and Mark W Reichelt. The matlab ode suite. *SIAM journal on scientific computing*, 18(1):1–22, 1997.

[17] Jon Peter Silverberg, Paul H Miller, and Joyce E Shade. *Performance Prediction of the Mk II Navy 44 Sail Training Craft with respect to Tank Testing, Velocity Prediction Programs, and Computational Fluid Dynamics*. Citeseer, 2003.

[18] Jean-Baptiste Souppez, JM Dewavrin, F Gohier, and G Borba Labi. Hydrofoil configurations for sailing superyachts: Hydrodynamics, stability and performance. 2019.

[19] M Leroy Spearman. Wind-tunnel investigation of an naca 0009 airfoil with 0.25-and 0.50-airfoil-chord plain flaps tested independently and in combination. Technical report, 1948.

[20] Zsolt Ugray, Leon Lasdon, John Plummer, Fred Glover, James Kelly, and Rafael Martí. Scatter search and local nlp solvers: A multistart framework for global optimization. *INFORMS Journal on computing*, 19(3):328–340, 2007.

[21] Richard A Waltz, José Luis Morales, Jorge Nocedal, and Dominique Orban. An interior algorithm for nonlinear optimization that combines line search and trust region steps. *Mathematical programming*, 107(3):391–408, 2006.

Appendices

Appendix A

Moving Mass Actuation

The derivation in this section largely follows much of the concept described in Chapter 3 with some modification to account for the moving masses. The body and inertial reference frame for the hydrofoil craft with moving mass actuation are shown in Figure A.1. For pitch

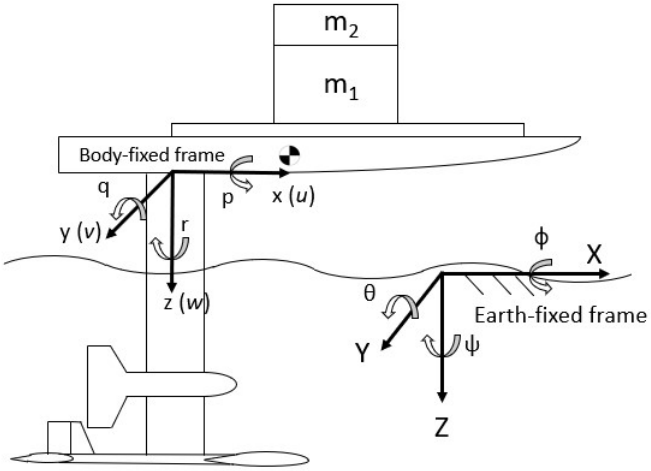

Figure A.1: Frame of reference for craft with moving masses

control, weights with mass m_1 and m_2 both moves in body-fixed x axis. For roll control, only the top weight with mass m_2 moves in the body-fixed y axis. For deriving the equation of motion, the position vectors shown in Figure A.2 are used where r_o is the inertial position vector to the body frame origin, r_c is the inertial position vector to the vehicle CoG, and r_G is the body-fixed position vector from body frame origin to the CoG. The position vector r_G

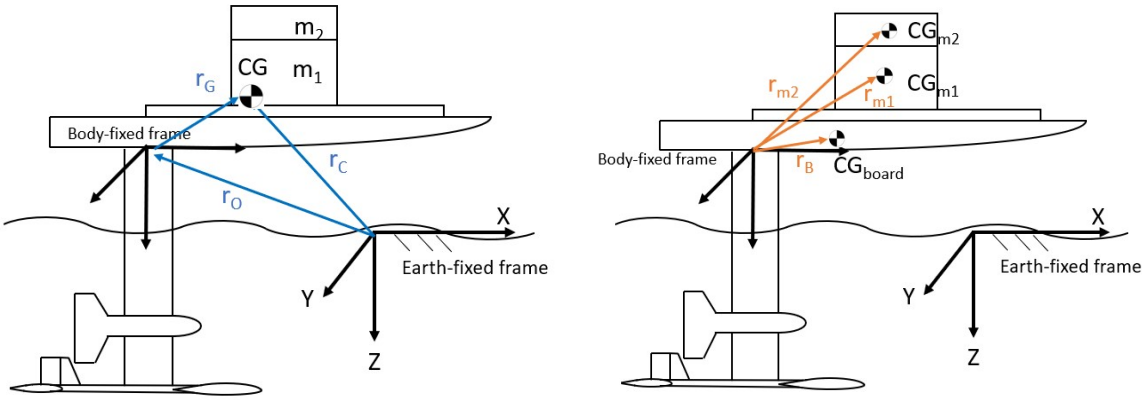

(a) Vector for overall vehicle CoG

(b) Vector for coG of moving masses in body frame

Figure A.2: Position vector for vehicle with moving mass actuation in inertial and body frame

can be described by the equation

$$r_G = \frac{m_B r_B + m_1 r_{m_1} + m_2 r_{m_2}}{m_B + m_1 + m_2} \tag{A.1}$$

where m_B is the masses of the eFoil assembly, r_B is the position vector to the eFoil's CoG, $r_{m_1} = [x_1, y_1, z_1]^T$ is the vector to CoG of the moving mass m_1 , and $r_{m_2} = [x_2, y_2, z_2]^T$ is the vector to CoG of the moving mass m_2 in the body frame as illustrated in Figure A.2. Because the eFoil assembly is assumed to be a rigid body, r_B is constant while r_{m_1} and r_{m_1} varies. Using conservation of linear momentum, applied force is related to the vehicle acceleration by

$$F = \dot{p} = M\dot{v}_c \tag{A.2}$$

where p is the vehicle linear momentum, $M = m_B + m_1 + m_2$ is the overall vehicle mass, and $v_c = \dot{r_c}$ is the velocity at the vehicle CoG. To find the expression for $\dot{v}_c$, we first use the

relations

$$\begin{aligned} r_c &= r_o + r_G \\ \dot{r}_c &= \dot{r}_o + \dot{r}_G \\ v_c &= \dot{r}_o + \dot{r}_G \end{aligned} \tag{A.3}$$

The expression for derivative of some vector x is given by

$$\dot{x} = \mathring{x} + w \times x \tag{A.4}$$

where $\dot{x}$ is the derivative in respect to Earth-fixed frame, $\mathring{x}$ is the derivative in respect to body-fixed frame, and w is rotation rate around body frame origin. Applying the relation in Equation A.4 to A.3 yields

$$v_c = v_o + \mathring{r}_G + w \times r_G \tag{A.5}$$

in which $\dot{r}_o = v_o$. For the case of flap actuation, $\mathring{r}_G$ is 0 since the vehicle CoG does not change, however, for moving mass, it is expressed as

$$\mathring{r}_G = \frac{m_1 \mathring{r}_{m_1} + m_2 \mathring{r}_{m_2}}{M} = \frac{m_1 v_{m_1} + m_2 v_{m_2}}{M} \tag{A.6}$$

Let $v_G = \mathring{r}_G$ then take derivative of v_c to get

$$\begin{aligned} \dot{v}_c &= \dot{v}_o + \dot{v}_G + \dot{w} \times r_G + w \times \dot{r}_G \\ \dot{v}_c &= (\mathring{v}_o + w \times v_o) + (\mathring{v}_G + w \times v_G) + \dot{w} \times r_G + w \times (\mathring{r}_G + w \times r_G) \\ \dot{v}_c &= \mathring{v}_o + w \times v_o + \mathring{v}_G + 2(w \times v_G) + \dot{w} \times r_G + w \times (w \times r_G) \end{aligned} \tag{A.7}$$

where $\mathring{v}_G$ is

$$\mathring{v}_G = \frac{m_1 \mathring{v}_{m_1} + m_2 \mathring{v}_{m_2}}{M} \tag{A.8}$$

Note that for angular velocity $w = [p, q, r]^T$, the derivative in respect to the inertial frame is same as the derivative in respect to the body frame since $\dot{w} = \mathring{w} + w \times w = \mathring{w}$. Some simplifications shown below can also be made for the vectors r_{m_1} and r_{m_2} based on the following assumptions: m_1 and m_2 does not move in the z axis, m_1 and m_2 move together in the x axis, and m_1 moves does not move in the y axis

$$\begin{aligned} r_{m1} &= \begin{bmatrix} x_1 \\ y_1 \\ z_1 \end{bmatrix} \qquad v_{m1} = \begin{bmatrix} v_x \\ 0 \\ 0 \end{bmatrix} \qquad \mathring{v}_{m1} = \begin{bmatrix} \mathring{v}_x \\ 0 \\ 0 \end{bmatrix} \\ r_{m2} &= \begin{bmatrix} x_1 \\ y_2 \\ z_2 \end{bmatrix} \qquad v_{m2} = \begin{bmatrix} v_x \\ v_y \\ 0 \end{bmatrix} \qquad \mathring{v}_{m2} = \begin{bmatrix} \mathring{v}_x \\ \mathring{v}_y \\ 0 \end{bmatrix} \end{aligned} \tag{A.9}$$

Using the vectors in Equation A.9 and plugging in A.7 to A.2 gives the transnational rigid body motion equation

$$\begin{bmatrix} F_x \\ F_y \\ F_z \end{bmatrix} = M\Bigg(\begin{bmatrix} \mathring{u} \\ \mathring{v} \\ \mathring{w} \end{bmatrix} + \begin{bmatrix} p \\ q \\ r \end{bmatrix} \times \begin{bmatrix} u \\ v \\ w \end{bmatrix} + \frac{1}{M} \begin{bmatrix} (m_1 + m_2)\mathring{v}_x \\ m_2 \mathring{v}_y \\ 0 \end{bmatrix} + 2\Big(\begin{bmatrix} p \\ q \\ r \end{bmatrix} \times \frac{1}{M} \begin{bmatrix} (m_1 + m_2)v_x \\ m_2 v_y \\ 0 \end{bmatrix} \Big) + \begin{bmatrix} \mathring{p} \\ \mathring{q} \\ \mathring{r} \end{bmatrix} \times \frac{1}{M} \begin{bmatrix} m_B x_B + m_1 x_1 + m_2 x_1 \\ m_B y_B + m_1 y_1 + m_2 y_2 \\ m_B z_B + m_1 z_1 + m_2 z_2 \end{bmatrix} + \begin{bmatrix} p \\ q \\ r \end{bmatrix} \times \Big(\begin{bmatrix} p \\ q \\ r \end{bmatrix} \times \frac{1}{M} \begin{bmatrix} m_B x_B + m_1 x_1 + m_2 x_1 \\ m_B y_B + m_1 y_1 + m_2 y_2 \\ m_B z_B + m_1 z_1 + m_2 z_2 \end{bmatrix} \Big) \Bigg) \tag{A.10}$$

For the rotational motion, we use the total angular momentum about the body frame origin h_O which is defined by [4]

$$h_O \triangleq \int_V r \times v \, \rho \, dV \tag{A.11}$$

where ρ is the density, r is the position vector in body fixed frame to a differential volume element dV with velocity v as shown in Figure A.3 Differentiating the angular momentum

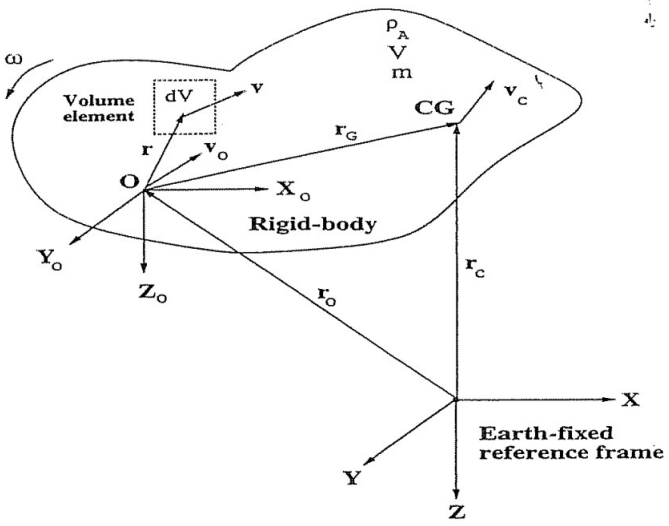

Figure A.3: Differential volume element in respect to body-fixed rotating frame [4]

gives

$$\dot{h}_O = \int_V r \times \dot{v}\, \rho\, dV + \int_V \dot{r} \times v\, \rho\, dV \tag{A.12}$$

The first integral term in Equation A.12 is the total moment applied on the body about the body origin M_O. The velocity vector used in the second integral term in Equation A.12 can be expressed as

$$v = \dot{r}_o + \dot{r} = v_o + \dot{r} \tag{A.13}$$

Since $\dot{r} \times \dot{r} = 0$ and v_o does not depend on the differential volume, the angular momentum derivative is

$$\dot{h}_O = M_o + \int_V \dot{r}\rho\, dV \times v_o \tag{A.14}$$

Using the definition of r_G and its derivative given by

$$\begin{aligned} r_G &= \frac{1}{M} \int_V r\rho\, dV \\ \dot{r}_G &= \frac{1}{M} \int_V \dot{r}\rho\, dV \end{aligned} \tag{A.15}$$

Equation A.14 simplifies to

$$\begin{aligned} \dot{h}_O &= M_o + M\dot{r}_G \times v_o \\ \dot{h}_O &= M_o + M(\mathring{r}_G + w \times r_G) \times v_o \\ \dot{h}_O &= M_o + M\mathring{r}_G \times v_o + M(w \times r_G) \times v_o \end{aligned} \tag{A.16}$$

Alternatively, angular momentum in Equation A.11 can be expressed as follows using Equation A.13

$$\begin{aligned} h_O &= \int_V r \times (v_o + \dot{r})\, \rho\, dV \\ h_O &= \int_V r \times v_o\, \rho\, dV + \int_V r \times \dot{r}\, \rho\, dV \\ h_O &= \int_V r\, \rho\, dV \times v_o + \int_V r \times (\mathring{r} + w \times r)\, \rho\, dV \\ h_O &= \int_V r\, \rho\, dV \times v_o + \int_V r \times \mathring{r}\, \rho\, dV + \int_V r \times (w \times r)\, \rho\, dV \end{aligned} \tag{A.17}$$

Plugging in A.15 and the definition $\int_V r \times (w \times r)\, \rho\, dV = I_o w$ where I_o is the moment of inertia around the body origin,

$$h_O = Mr_G \times v_o + \int_V r \times \mathring{r}\, \rho\, dV + I_o w \tag{A.18}$$

Noting that $\mathring{r}$ is nonzero only for differential volume of the moving masses and that all volume elements in mass 1 and mass 2 has the same velocity in repsect to body-fixed origin, we can rewrite $r \times \mathring{r}$ as

$$\int_V r \times \mathring{r}\, \rho\, dV = \int_{m_1} r\, \rho\, dV \times v_{m_1} + \int_{m_2} r\, \rho\, dV \times v_{m_2} = m_1 r_{m_1} \times v_{m_1} + m_2 r_{m_2} \times v_{m_2} \tag{A.19}$$

Substituting A.19 into A.18 and taking the derivative yields

$$\begin{gathered}\dot{h}_O = M\dot{r}_G \times v_O + Mr_G \times \dot{v}_O + m_1\dot{r}_{m1} \times v_{m1} + m_1 r_{m1} \times \dot{v}_{m1} + m_2\dot{r}_{m2} \times v_{m2} + \\ m_2 r_{m2} \times \dot{v}_{m2} + (\dot{I_O}w) \\ \dot{h}_O = M\mathring{r}_G \times v_O + M(w \times r_G) \times v_O + Mr_G \times \mathring{v}_O + Mr_G \times (w \times v_O) + \\ m_1(w \times r_{m1}) \times v_{m1} + m_1 r_{m1} \times \mathring{v}_{m1} + m_1 r_{m1} \times (w \times v_{m1}) + m_2(w \times r_{m2}) \times v_{m2} + \\ m_2 r_{m2} \times \mathring{v}_{m2} + m_2 r_{m2} \times (w \times v_{m2}) + (\dot{I_O}w)\end{gathered} \tag{A.20}$$

We now have two expressions for derivative of angular momentum. Setting Equation A.16 and A.20 to each other and solving for the moment M_o around body fixed origin gives

$$\begin{gathered}M_o = Mr_G \times \mathring{v}_O + Mr_G \times (w \times v_O) + m_1(w \times r_{m1}) \times v_{m1} + m_1 r_{m1} \times \mathring{v}_{m1} + \\ m_1 r_{m1} \times (w \times v_{m1}) + m_2(w \times r_{m2}) \times v_{m2} + m_2 r_{m2} \times \mathring{v}_{m2} + m_2 r_{m2} \times (w \times v_{m2}) + \\ \mathring{I}_o w + I_o \mathring{w} + w \times (I_o w)\end{gathered} \tag{A.21}$$

The inertia tensor $I_o = I_B + I_{m_1} + I_{m_2}$ is composed of the moment of inertia for the eFoil I_B, which does not change, and the moment of inertia for the moving masses I_{m_1} and I_{m_2}. We can use the parallel axis theorem to derive the moment of inertia for the moving masses as

$$\begin{aligned}I_{m_1} &= I_{CG_{m1}} + m_1 \begin{bmatrix} y_1^2 + z_1^2 & -x_1 y_1 & -x_1 z_1 \\ -y_1 x_1 & x_1^2 + z_1^2 & -y_1 z_1 \\ -z_1 x_1 & -z_1 y_1 & x_1^2 + y_1^2 \end{bmatrix} \\ I_{m_2} &= I_{CG_{m2}} + m_2 \begin{bmatrix} y_2^2 + z_2^2 & -x_1 y_2 & -x_1 z_2 \\ -y_2 x_1 & x_1^2 + z_2^2 & -y_2 z_2 \\ -z_2 x_1 & -z_2 y_2 & x_1^2 + y_2^2 \end{bmatrix}\end{aligned} \tag{A.22}$$

where $I_{CG_{m_1}}$ and $I_{CG_{m_2}}$ are the inertia tensor of mass 1 and mass 2 about their own center of gravity which are constant. Note that only x_1 and y_2 change with time as those are the

only axes where the moving masses are assumed to move. Taking the derivative of I_o ins respect to the body frame gives

$$\mathring{I}_o = m_1 \begin{bmatrix} 0 & -y_1\mathring{x}_1 & -z_1\mathring{x}_1 \\ -y_1\mathring{x}_1 & 2x_1\mathring{x}_1 & 0 \\ -z_1\mathring{x}_1 & 0 & 2x_1\mathring{x}_1 \end{bmatrix} + m_2 \begin{bmatrix} 2y_2\mathring{y}_2 & -y_2\mathring{x}_1 - x_2\mathring{y}_2 & -z_2\mathring{x}_1 \\ -y_2\mathring{x}_1 - x_2\mathring{y}_2 & 2x_2\mathring{x}_1 & -z_2\mathring{y}_2 \\ -z_2\mathring{x}_1 & -z_2\mathring{y}_2 & 2x_2\mathring{x}_1 + 2y_2\mathring{y}_2 \end{bmatrix}$$
$$= \begin{bmatrix} 2m_2y_2\mathring{y}_2 & -(m_1y_1 + m_2y_2)\mathring{x}_1 - m_2x_2\mathring{y}_2 & -(m_1z_1 + m_2z_2)\mathring{x}_1 \\ -(m_1y_1 + m_2y_2)\mathring{x}_1 - m_2x_2\mathring{y}_2 & 2(m_1x_1 + m_2x_2)\mathring{x}_1 & -m_2z_2\mathring{y}_2 \\ -(m_1z_1 + m_2z_2)\mathring{x}_1 & -m_2z_2\mathring{y}_2 & 2(m_1x_1 + m_2x_2)\mathring{x}_1 + 2m_2y_2\mathring{y}_2 \end{bmatrix} \tag{A.23}$$

Plugging in A.23 and the vectors in A.9 to Equation A.21 gives the rotational rigid body motion equation

$$\begin{bmatrix} M_x \\ M_y \\ M_z \end{bmatrix} = M\left(\frac{1}{M} \begin{bmatrix} m_Bx_B + m_1x_1 + m_2x_2 \\ m_By_B + m_1y_1 + m_2y_2 \\ m_Bz_B + m_1z_1 + m_2z_2 \end{bmatrix} \times \begin{bmatrix} \mathring{u} \\ \mathring{v} \\ \mathring{w} \end{bmatrix} + \frac{1}{M} \begin{bmatrix} m_Bx_B + m_1x_1 + m_2x_2 \\ m_By_B + m_1y_1 + m_2y_2 \\ m_Bz_B + m_1z_1 + m_2z_2 \end{bmatrix} \times \left(\begin{bmatrix} p \\ q \\ r \end{bmatrix} \times \begin{bmatrix} u \\ v \\ w \end{bmatrix} \right) \right) +$$
$$m_1\left(\begin{bmatrix} p \\ q \\ r \end{bmatrix} \times \begin{bmatrix} x_1 \\ y_1 \\ z_1 \end{bmatrix} \right) \times \begin{bmatrix} v_x \\ 0 \\ 0 \end{bmatrix} + m_1 \begin{bmatrix} x_1 \\ y_1 \\ z_1 \end{bmatrix} \times \begin{bmatrix} \mathring{v}_x \\ 0 \\ 0 \end{bmatrix} + m_1 \begin{bmatrix} x_1 \\ y_1 \\ z_1 \end{bmatrix} \times \left(\begin{bmatrix} p \\ q \\ r \end{bmatrix} \times \begin{bmatrix} v_x \\ 0 \\ 0 \end{bmatrix} \right) + m_2\left(\begin{bmatrix} p \\ q \\ r \end{bmatrix} \times \begin{bmatrix} x_1 \\ y_2 \\ z_2 \end{bmatrix} \right) \times \begin{bmatrix} v_x \\ v_y \\ 0 \end{bmatrix} +$$
$$m_2 \begin{bmatrix} x_1 \\ y_2 \\ z_2 \end{bmatrix} \times \begin{bmatrix} \mathring{v}_x \\ \mathring{v}_y \\ 0 \end{bmatrix} + m_2 \begin{bmatrix} x_1 \\ y_2 \\ z_2 \end{bmatrix} \times \left(\begin{bmatrix} p \\ q \\ r \end{bmatrix} \times \begin{bmatrix} v_x \\ v_y \\ 0 \end{bmatrix} \right) + \begin{bmatrix} I_x & -I_{xy} & -I_{xz} \\ -I_{yx} & I_y & -I_{yz} \\ -I_{zx} & -I_{zy} & I_z \end{bmatrix} \begin{bmatrix} \mathring{p} \\ \mathring{q} \\ \mathring{r} \end{bmatrix} + \begin{bmatrix} p \\ q \\ r \end{bmatrix} \times \begin{bmatrix} I_xp - I_{xy}q - I_{xz}r \\ -I_{yx}p + I_yq - I_{yz}r \\ -I_{zx}p - I_{zy}q + I_zr \end{bmatrix}$$
$$\begin{bmatrix} 2m_2y_2\mathring{y}_2 & -(m_1y_1 + m_2y_2)\mathring{x}_1 - m_2x_2\mathring{y}_2 & -(m_1z_1 + m_2z_2)\mathring{x}_1 \\ -(m_1y_1 + m_2y_2)\mathring{x}_1 - m_2x_2\mathring{y}_2 & 2(m_1x_1 + m_2x_2)\mathring{x}_1 & -m_2z_2\mathring{y}_2 \\ -(m_1z_1 + m_2z_2)\mathring{x}_1 & -m_2z_2\mathring{y}_2 & 2(m_1x_1 + m_2x_2)\mathring{x}_1 + 2m_2y_2\mathring{y}_2 \end{bmatrix} \begin{bmatrix} p \\ q \\ r \end{bmatrix} \tag{A.24}$$

Using the modified state vector $\nu = \begin{bmatrix} u & v & w & p & q & r & x_1 & y_2 & \dot{x}_1 & \dot{x}_2 \end{bmatrix}^T$ where the body frame positions of the moving masses x_1 and y_2 and body frame velocities of the moving masses $\dot{x}_1$ and $\dot{y}_2$ are added, we can define new rigid body inertia and Coriolis-centripetal

matrices for the moving mass system as

$$M_{RB} = \begin{bmatrix} M & 0 & 0 & 0 & z_M & -y_M & 0 & 0 & (m_1+m_2) & 0 \\ 0 & M & 0 & -z_M & 0 & x_M & 0 & 0 & 0 & m_2 \\ 0 & 0 & M & y_M & -x_M & 0 & 0 & 0 & 0 & 0 \\ 0 & -z_M & y_M & I_x & -I_{xy} & -I_{xz} & 0 & 0 & 0 & -m_2 z_2 \\ z_M & 0 & -x_M & -I_{yx} & I_y & -I_{yz} & 0 & 0 & (m_1 z_1 + m_2 z_2) & 0 \\ -y_M & x_M & 0 & -I_{zx} & -I_{zy} & I_z & 0 & 0 & -(m_1 y_1 + m_2 y_2) & m_2 x_1 \\ 0 & 0 & 0 & 0 & 0 & 0 & 1 & 0 & 0 & 0 \\ 0 & 0 & 0 & 0 & 0 & 0 & 0 & 1 & 0 & 0 \\ 0 & 0 & 0 & 0 & 0 & 0 & 0 & 0 & (m_1+m_2) & 0 \\ 0 & 0 & 0 & 0 & 0 & 0 & 0 & 0 & 0 & m_2 \end{bmatrix} \tag{A.25}$$

$$C_{RB} = \begin{bmatrix} 0 & 0 & 0 & y_M q + z_M r & -x_M q + M w & -x_M r - M v \\ 0 & 0 & 0 & -y_M p - M w & z_M r + x_M p & -y_M r + M u \\ 0 & 0 & 0 & -z_M p + M v & -z_M q - M u & x_M p + y_M q \\ -y_M q - z_M r & y_M p & z_M p & 0 & -I_{zx} p - I_{zy} q + I_z r & I_{yx} p - I_y q + I_{yz} r \\ x_M q & -z_M r - x_M p & z_M q & I_{zx} p + I_{zy} q - I_z r & 0 & I_x p - I_{xy} q - I_{xz} r \\ x_M r & y_M r & -x_M p - y_M q & -I_{yx} p + I_y q - I_{yz} r & -I_x p + I_{xy} q + I_{xz} r & \\ 0 & 0 & 0 & 0 & 0 & 0 \\ 0 & 0 & 0 & 0 & 0 & 0 \\ 0 & 0 & 0 & 0 & 0 & 0 \\ 0 & 0 & 0 & 0 & 0 & 0 \end{bmatrix}$$

$$\begin{bmatrix} 0 & 0 & 0 & -2m_2 r \\ 0 & 0 & (2m_1+2m_2)r & 0 \\ 0 & 0 & -(2m_1+2m_2)q & 2m_2 p \\ 0 & 0 & -(2m_1 y_1 + 2m_2 y_2)q - (2m_1 z_1 + 2m_2 z_2)r & 2m_2 y_2 p \\ 0 & 0 & (2m_1 x_1 + 2m_2 x_2)q & -(2m_2 x_2 p + 2m_2 z_2 r) \\ 0 & 0 & (2m_1 x_1 + 2m_2 x_2)r & 2m_2 y_2 r \\ 0 & 0 & -1 & 0 \\ 0 & 0 & 0 & -1 \\ 0 & 0 & 0 & 0 \\ 0 & 0 & 0 & 0 \end{bmatrix} \tag{A.26}$$

With the above definitions for ν, M_{RB}, and C_{RB}, Equation 3.4 can still be used to describe the moving mass system with slight modifications to the τ term which include the addition of the weight contribution of m_1 and m_2 in the restoring forces and moments vector, actuator forces in x and y axis to move the masses, and some frictional loss of the moving mass system

that can be modeled to be proportional to the velocity of m_1 and m_2.

Appendix B

Vehicle Specification

Table B.1: Component CoG in Body Reference Coordinate and Weight

Component	CoG $[x, y, z]$ (m)	Weight (Kg)
eFoil Board with Mounting Rail	[0.526, 0, -0.081]	14.7
eFoil Controller Board	[-0.15, 0, -0.047]	4.8
eFoil Battery	[0.3, 0, -0.053]	12.5
Strut & Propulsor Assembly	[-0.087, 0, 0.511]	4.75
Front and Rear Hydrofoil	[0.09, 0, 0.733]	2.54
Autonomy Electronics Box	[1.05, 0, -0.29]	7.61
Flap Actuator Assembly	[-0.269, 0, 0.73]	0.97